

# ISOCAM survey and dust models of 3CR radio galaxies and quasars<sup>\*</sup>

R. Siebenmorgen<sup>1</sup>, W. Freudling<sup>2,1</sup>, E. Krügel<sup>3</sup>, and M. Haas<sup>4</sup>

<sup>1</sup> European Southern Observatory, Karl-Schwarzschildstr. 2, D-85748 Garching b. München

<sup>2</sup> Space Telescope – European Coordinating Facility, Karl-Schwarzschildstr. 2, D-85748 Garching b. München

<sup>3</sup> Max-Planck-Institut für Radioastronomie, Auf dem Hügel 69, Postfach 2024, D-53010 Bonn

<sup>4</sup> Astronomisches Institut, Ruhr-Universität, Universitätsstr. 150, D-44780 Bochum

Received 22 December 2003 / Accepted 18 March 2004

**Abstract.** We present a survey of all 3CR sources imaged with ISOCAM onboard the *Infrared Space Observatory* (ISO). The sample consists mostly of radio-loud active galactic nuclei (AGN). For each source, we present spatially integrated mid-infrared (MIR, 5 – 18 $\mu$ m) fluxes measured from newly calibrated ISOCAM images. In total, we detected 68 objects of the 3CR catalogue, at redshifts  $z \leq 2.5$ , and obtained upper limits for 17 objects. In addition, we detected 10 galaxies not listed in the 3CR catalogue. The one with the highest redshift is 4C+72.26 at  $z = 3.53$ . ISOCAM data are combined with other photometric measurements to construct the spectral energy distribution (SED) from optical to radio wavelengths. The MIR emission may include synchrotron radiation of the AGN, stars of the host galaxy or dust. Extrapolation of radio core fluxes to the MIR show that the synchrotron contribution is in most cases negligible. In order to describe dust emission we apply new radiative transfer models. In the models the dust is heated by a central source which emits photons up to energies of 1keV. By varying three parameters, luminosity, effective size and extinction, we obtain a fit to the SED for our objects. Our models contain also dust at large (several kpc) distance from the AGN. Such a cold dust component was neglected in previous computations which therefore underestimated the AGN contribution to the far infrared (FIR). In 53 cases ( $\sim 75\%$  of our detected 3CR sources), the MIR emission can be attributed to dust. The *hot dust* component is mainly due to small grains and PAHs. The modelling demonstrates that an AGN heating suffices to explain the ISO broad band data, starburst activity is not necessary. In the models, a type 1 AGN is represented by a compact dust distribution, the dust is therefore very warm and emission of PAHs is weak because of photo-destruction. In AGNs of type 2, the dust is relatively colder but PAH bands are strong.

**Key words.** Infrared: galaxies – Galaxies: ISM – Galaxies: dust

## 1. Introduction

More than 20 years ago Kotanyi & Ekers (1979) pointed out that for radio-loud elliptical galaxies, the orientation of the (optical) dust lane appears preferentially perpendicular to the radio axis. In unification theories dust plays an important role. In all of them, a supermassive black-hole accretes gas from a disk and, in radio-loud objects, a jet is ejected parallel to the rotation axis. The blackhole and the disk are surrounded by a torus of interstellar gas and dust which may block light from the central region on the way to the observer. The diversity in the appearance

of activity types is then explained foremost as a result of different viewing angles (Barthel 1989).

The obscuring dust torus is at the heart of unification theories. It reaches towards the blackhole as close as dust can survive ( $T \lesssim 1500$  K). As the torus is not directly seen on optical images, its dimensions are at most a few hundred parsec. Because of the immense bolometric luminosity emitted from the AGN, the dust in the torus, even at a distance of 100 pc, must be very warm ( $> 100$  K), and further in even *hot*. Such hot dust will emit preferentially in the mid infrared (MIR), at wavelengths covered by the ISOCAM filters.

Dust in radio galaxies is not restricted to the nuclear region, but is ubiquitous in the host galaxy. It absorbs and scatters the light, but also radiates thermally as it is heated either by the nucleus or by stars. Of course, the diffuse and spatially extended dust is much colder than the dust near the AGN. Rapid star formation is also a po-

Send offprint requests to: rsiebenm@eso.org

<sup>\*</sup> Based on observations with ISO, an ESA project with instruments funded by ESA Member States (especially the PI countries: France, Germany, the Netherlands and the United Kingdom) with the participation of ISAS and NASA.

tential heating source, besides the AGN. A detailed search for dust in the nuclear regions of 120 radio sources of the 3CR catalogue was carried out by de Koff et al. (2000) using optical HST images at  $0.7\mu\text{m}$  center wavelength and of  $0.1''$  resolution. In one out of three galaxies, they found evidence for dust obscuration, with a large variety of morphologies such as disks, lanes or filaments. Dust distributed smoothly on a large scale of several kpc is difficult to detect in absorption maps but reveals itself by infrared emission.

The dust shroud of an AGN is often not transparent and to model the emission spectrum one has to compute the radiative transfer. Models for optically thick dusty nuclei and galaxies have been carried out in various approximations (Pier & Krolik 1993, Laor & Draine 1993 Krügel & Siebenmorgen 1994, Granato & Danese 1994, Efstathiou & Rowan–Robinson 1995, Siebenmorgen et al. 1997, Nenkova et al. 2002, Popescu et al. 2004). Previous AGN dust models underestimated the FIR as they did not include dust located at large distances from the center and thus missed the cold component. To overcome the deficit emission in the FIR, these authors add an additional component to the models and attribute it to starburst activity (e.g. Rowan–Robinson 2000). In Section 4, we present AGN dust models where large scale dust emission is incorporated and where the geometry is radically simplified so that they can be described by only three parameters.

A cold dust component was discovered in 18 sources of the 3CR catalogue already by IRAS (Heckman et al. 1994) and more recently, in more objects, by ISOPHOT (Fanti et al. 2000, Meisenheimer et al. 2001, Van Bemmell et al. 2001, Andreani et al. 2002, Spinoglio et al. 2002, Haas et al. 2004). These authors detected also a few sources in the MIR. The hot dust responsible for it must be close to the nucleus and its detection serves as a further test for the unified model hypothesis. This motivated us to survey the 3CR galaxies in the MIR by means of ISOCAM images available from the ISO archive. The sensitivity of ISOCAM is 2 – 3 orders of magnitude greater than IRAS at  $12\mu\text{m}$ .

In Section 2 and 3, we present the images, pertaining photometric measurements as well as results. The spectral energy distributions (SED) are displayed in Section 4. To interpret them, we apply radiative transfer models. A discussion of generic SED properties in the infrared for different AGN types is given in Section 5. The conclusions are given in Section 6. In Appendix A we remark on individual galaxies (previous indications of dust, X-ray properties, jets, presence of high excitation lines, source morphology, companions). In Appendix B, we make for each galaxy a note on the radiative transfer models of Section 4. Details of the ISOCAM observational set up is summarised in Tab. B.1. The fully reduced and astrometrically corrected ISOCAM images are shown as overlays on optical images in Fig. B.

## 2. Survey data

We present the data of our survey, describe which ISOCAM fields were extracted from the ISO archive, briefly overview the ISOCAM observing modes, and outline data reduction, source identification and photometric procedures.

### 2.1. Source selection

The parent catalogue for our sample is the third update of the revised third Cambridge catalogue (3CR) by Spinrad et al. (1985). It contains 298 sources of which 195 are classified as radio galaxies and 53 as radio quasars. Most of the objects in the 3CR catalogue are well observed at optical and near infrared wavelengths. We searched in the ISO archive for ISOCAM (Cesarsky et al. 1996) observations made with the long wavelength array (LW). All ISOCAM images containing, potentially, at least, one 3CR source have been extracted. Altogether, we found 146 such ISOCAM observations. Often the same source was observed in multiple filter band passes. On the fully reduced ISOCAM images, we determined and improved the astrometric pointing by identifying objects with accurate coordinates listed in the SIMBAD Astronomical Database or the NASA/IPAC Extragalactic Database (NED). The images are presented in Fig. B. We also made 10 serendipitous detections of galaxies which are not members of the 3CR catalogue. They are eye-ball detections at the position of NED coordinates.

### 2.2. Observations

Most of the observations were done in the so called mini-raster mode where different ISOCAM detector pixels saw the same part of the sky (see ISO Handbook for a description of observing modes, Leech & Pollock, 2001). In addition, there are nine staring and one beam switch observation. Three observations were performed in the circular variable filter (CVF) scan mode and one in the polarimetric mode.

Depending on the lens used in the experiment, the pixel scale of the  $32 \times 32$  element detector was  $1.5''$ ,  $3''$  and  $6''$  and the total field of view  $48 \times 48$ ,  $96 \times 96$  and  $180 \times 180 \text{ arcsec}^2$ , respectively. The most frequently applied broad band filter was LW10 with a bandwidth from  $8\text{--}15\mu\text{m}$  and central wavelength at  $12\mu\text{m}$ . In addition there are observations with filter: LW1 ( $4\text{--}5$ ,  $4.5\mu\text{m}$ ), LW2 ( $5\text{--}8.5$ ,  $6.7\mu\text{m}$ ), LW3 ( $12\text{--}18$ ,  $14.3\mu\text{m}$ ), LW7 ( $8.5\text{--}11$ ,  $9.6\mu\text{m}$ ) and CVF scans ( $5\text{--}17\mu\text{m}$ ) at spectral resolution of  $\lambda/\Delta\lambda \approx 50$ . In a single observing template often more than one filter was selected.

Parameters of the observing templates are detailed in Tab. B.1: target dedicated time (TDT) by which the observations are identified (column 1), celestial coordinate of the map center (column 2 and 3), observing date (column 4), band pass filter (column 5), lens (column 6), number of raster points  $M$  (column 7) and raster lines  $N$  (col-

**Table 1.** ISOCAM photometry of 3CR sources

Name	TDT	Band $\mu\text{m}$	Flux mJy	RMS mJy
1	2	3	4	5
3C006.1	70101081	12.0	0.9	0.2
3C013	80801283	12.0	0.7	0.2
3C017	57502102	12.0	4.0	0.4
3C018	61901003	12.0	9.1	0.6
3C020	59702305	12.0	5.3	0.4
3C022	78500882	12.0	7.1	0.4
3C031	58703801	4.5	30	2
	40201422	6.7	36	2
	58703793	12.0	25	1
	58703801	14.3	30	2
3C033.1	59702607	12.0	18	1
3C048	43901804	14.3	59	4
3C061.1	56201411	12.0	4.3	0.3
3C66B	45304902	4.5	14	1
	43502724	6.7	13	1
	45304902	14.3	3.8	1.6
3C071	63301602	4.5	6860	340
(NGC1068)	63301902	6.8	14030	700
	63302202	14.9	50830	2540
3C076.1	46601603	4.5	5.1	1.0
	46601603	6.7	3.0	0.8
	46601603	14.3	1.0	1.5
3C079	61503807	12.0	21	2
3C083.1	65901304	4.5	31	2
	65901032	6.7	47	3
	65901304	14.3	9.7	1.5
3C084	61503617	6.7	230	20
		9.6	400	70
		14.3	1000	100
3C098	63302405	4.5	6.5	1.0
	63302405	6.7	7.7	0.9
	63302405	14.3	24	2
3C231	12300106	6.7	25000	1250
(M82)	12300106	12.0	63000	3150
	12300106	14.9	68000	3400
3C249.1	21305001	12.0	19	1
3C265	22400201	4.5	1.3	0.5
	22201802	6.7	2.4	0.2
	22400303	12.0	6.0	1.6
3C270	22801205	4.5	160	8
	22801205	6.7	95	5
	22801205	14.3	38	3
3C272.1	23502406	4.5	900	46
	23100414	6.7	240	12
	23100414	9.6	150	8
	23100414	14.3	53	3
3C273	24100504	14.3	290	15
	24100504	6.7	190	10
3C274	23800308	4.5	740	38
(M87)	23800308	6.7	260	13
	23901834	12.0	51	3
3C277.3	24500106	6.7	3.6	0.3
	24500106	14.3	8.5	0.5

**Table 1.** - continued.

Name	TDT	Band $\mu\text{m}$	Flux mJy	RMS mJy
1	2	3	4	5
3C286	38800808	12.0	3.6	0.3
3C288.1	24407233	12.0	2.3	0.6
3C293	61701307	4.5	16	1
	61701307	6.7	14	1
	61701413	12.0	19	2
	61701307	14.3	23	1
3C295	18001405	6.7	1.4	0.3
3C296	27000606	4.5	30	2
	27000606	6.7	16	1
	27000606	14.3	13	1
3C303.1	52900115	12.0	1.9	0.2
3C305	46300408	4.5	12	1
	12300205	6.7	7.1	2.7
	51400760	12.0	21	1
	12300205	14.3	27	5
3C305.1	71702771	12.0	1.5	0.2
3C309.1	60001472	12.0	8.2	0.5
	60092200	6.7	4.4	0.5
3C319	54100619	12.0	1.3	0.2
3C321	65800208	6.7	12	1
	65800208	12.0	27	1
	65800208	14.4	51	3
3C324	30300612	6.7	0.1	0.2
	30300413	12.0	1.7	0.2
3C330	33600323	6.7	1.3	0.2
	60001373	12.0	1.7	0.2
	33600323	14.3	2.6	0.5
3C332	60201725	12.0	9.2	0.5
3C336	30400442	12.0	2.4	0.5
	30492200	6.7	0.9	0.2
3C338	10601408	4.5	16	1
	10601408	6.7	9.4	0.8
	51100561	12.0	8.8	0.5
	10601408	14.3	7.3	1.4
3C341	60201626	12.0	8.0	0.5
3C343	61900565	12.0	1.4	0.2
3C345	51100679	12.0	22	1
3C346	64001327	12.0	4.2	0.3
3C349	52500429	12.0	3.4	0.3
3C351	52500130	12.0	32	2
3C356	52100668	12.0	0.6	0.2
3C371	52901232	12.0	66	4
	55500476	14.3	91	5
3C379.1	52901433	12.0	3.6	0.3
3C380	54100969	12.0	14	1
3C381	50304334	12.0	19	1
3C382	52500562	12.0	85	5
3C386	47100710	4.5	13	1
	47100710	6.7	6.3	0.8
	51301035	12.0	5.6	0.3
	47100710	14.3	3.3	1.4
3C388	54100836	12.0	1.2	0.2
3C390.3	52901537	12.0	94	5

**Table 1.** - continued.

Name	TDT	Band $\mu\text{m}$	Flux mJy	RMS mJy
1	2	3	4	5
3C402	49604639	12.0	3.4	0.5
3C410	53503041	12.0	22	1
3C418	54101870	12.0	3.6	0.3
3C430	54301344	12.0	1.7	0.3
3C433	52201845	12.0	32.0	2
3C445	54500518	6.7	93	5
	54500518	14.3	210	11
3C449	54801112	4.5	16	1
	36701710	6.7	10	1
	37403041	12.0	7.6	0.9
	54801252	12.0	8.7	0.5
	36701710	14.3	11	2
3C452	54801053	12.0	23	1
3C456	54700854	12.0	9.1	0.6
3C459	37500303	4.5	0.1	0.5
		6.0	5.5	0.9
		7.7	6.8	1.1
		14.9	29.5	4.0
3C465	39501112	4.5	22	1
	39501112	6.7	8.1	0.8
3C469.1	56201064	12.0	1.8	0.2

umn 8), step between raster points  $dM$  (column 9) and raster lines  $dN$  (column 10), both in arcsec, and the median number of exposures taken on each raster position (column 11) together with the integration time per read-out (column 12).

### 2.3. Data reduction

The data were reduced with the ISOCAM Interactive Analysis (CIA, Ott et al. 1996). We used the default data reduction steps of CIA: dark current subtraction, initial removal of cosmic ray hits (glitches), detector transient fitting, exposure coaddition, flat fielding and flux conversion to astronomical units. Except for staring modes, the coadded images at each raster position were sky projected and corrected for field distortion.

The dark current depends on the orbital position of the ISO space-craft and the temperature of the ISOCAM detector. The applied correction is based on a model described by Roman & Ott (1998). The deglitching is done by following the temporal signal variation of a pixel using a multi-resolution wavelet transform algorithm (Starck et al. 1997). The response of the detector pixels depends on the previous observations and there may be long term hysteresis effects for each detector element after changes of the photon flux level. We applied the detector flux transient fitting method for ISOCAM data (Coulais & Abergel 2000). After application of the default deglitcher some

**Table 2.** ISOCAM  $3\sigma$  upper limits of 3CR sources

Name	TDT	Band $\mu\text{m}$	Flux mJy
1	2	3	4
3C002	41907203	12.0	<1.7
3C313	08800387	12.0	<6.2
3C314.1	52900417	12.0	<0.6
3C320	59501620	12.0	<0.5
3C343.1	39901248	12.0	<3.3
3C352	51800667	12.0	<0.6
3C357	51800831	12.0	<0.6
3C368	71200283	6.7	<1.5
	10200421	6.7	<8.1
	71200283	14.3	<2.1
3C401	53200838	12.0	<0.6
3C427.1	52902663	12.0	<0.6
3C434	53503146	12.0	<1.0
3C436	52201948	12.0	<1.0
3C437	53503288	12.0	<1.4
3C438	54000949	12.0	<0.5
3C442	53702911	14.3	<4.5
3C454.1	56001074	12.0	<0.6
3C460	56501357	12.0	<0.4

residuals of cosmic ray impacts were still visible in the data. Therefore we applied after the detector flux transient correction a second cosmic ray rejection method which is basically a multi-sigma clipping of the temporal signal (Ott et al. 2000). For raster observations, flat field estimation can be improved by an iterative method exploiting the fact that the same sky area is seen by different detector pixels (Starck et al. 1999). The method works best for highly redundant data where a large number of pixels see the same sky. In case of low redundancy rasters and for staring observations, we flat-fielded according to the standard calibration library.

### 2.4. Source photometry

To determine the source flux, we perform a multi-aperture photometry. For each aperture centered on the brightest pixel of the source we determine the background as the mean flux derived in a 4 pixel wide annulus which is put 2 pixels away from the greatest ( $\sim 18''$ ) aperture. In this way, we obtain aperture fluxes that flatten with increasing aperture radius and approach an asymptotic value. For point sources the same procedure is repeated on a theoretical and normalised point source image (Okumura 1998) to find the correction factor of the multi-aperture analysis. The correction factor is typically 5%. The determination if a source is a point source or not is done by eye. The procedure will introduce an error of less than the correction factor for slightly extended sources misjudged to be a point source. In order to derive the statistical flux

**Table 3.** ISOCAM photometry of galaxies not in the 3CR catalogue

Name	TDT	Band $\mu\text{m}$	Flux mJy	RMS mJy
1	2	3	4	5
4C+72.26	74101506	12.0	0.7	0.08
NGC0382	58703801	4.5	7.0	1.2
	40201422	6.7	12	2
	58703793	12.0	7.3	0.5
	58703801	14.3	10	2
NGC7236	53702911	6.7	3.8	0.8
	53702750	12.0	2.8	0.3
	53702911	14.3	5.5	1.5
NGC7237	53702911	6.7	3.6	0.8
	53702750	12.0	1.8	0.2
NGC5532NED02	27000606	4.5	4.5	1.0
	27000606	6.7	1.0	0.8
F17130+5021	52100804	12.0	14	1
J1728201+314603	51800831	12.0	2.8	0.2
PMNJ0214-11582	59601514	12.0	1.8	0.3
PGC012293	65901032	6.7	1.3	0.2
	65901304	14.3	3.0	1.4
PCd91212130.83+	35701635	6.7	31	2
	245139.2			

uncertainty, for the source aperture we quadratically add the RMS image and the  $1\sigma$  uncertainty of the background estimate. The systematic error of ISOCAM photometry is typically  $\lesssim 5\%$  and color corrections of order 10% (see ISOCAM Handbook, Blommaert et al. 2001).

### 3. Results

We find from the detection statistics of the ISOCAM survey of 3CR sources that in our sample there is no bias against AGN type. We present SEDs from optical to radio wavelengths for individual sources and discuss potential contributions to the ISOCAM fluxes (synchrotron, photospheric and dust emission).

#### 3.1. Bias and detection statistics

The primary goal of our survey is to compile a sample of radio-loud AGNs which is not subjects to biases related to the type and therefore viewing angle of the AGN torus. While this seems to be the case for the parent 3CR catalogue (e.g. Urry and Piovani 1995), the selection of objects from the ISOCAM survey was beyond our control. We shall therefore compare the flux and redshift distribution of the galaxies detected by ISOCAM with those of the 3CR catalogue.

In total, we detected 68 sources from the 3CR catalogue and determined 17 upper limits up to redshifts  $z \leq 2.5$ . Furthermore, there are 10 serendipitous detections of galaxies in the ISOCAM images which are not

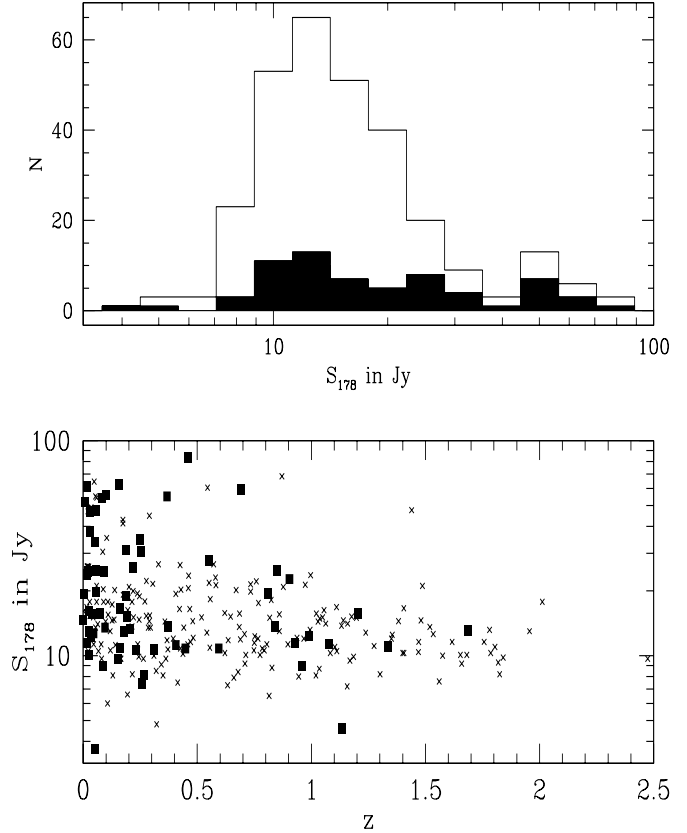


**Fig. 1.** Top: Histogram of the distribution of the 178 MHz radio fluxes in the 3CR catalogue. The filled part represents the objects detected by ISOCAM. Bottom: Radio fluxes of 3CR sources at 178 MHz plotted as a function of redshift. The filled squares are objects of this paper.

listed in the 3CR catalogue. One example is the radio source 4C+72.26 at redshift  $z = 3.53$ . The ISOCAM fluxes of detected 3CR sources are listed in Tab. 1 and upper limits of non-detected 3CR sources in Tab. 2. We also give the ISOCAM flux for galaxies which are not members of the 3CR catalogue in Tab. 3. Notations in Tab. 1 and Tab. 3 are: catalogue name (column 1), the TDT number used as an identifier of the observation is listed in column 2, followed by the central wavelength ( $\mu\text{m}$ ) of the filter band pass (column 3), aperture flux (column 4) and  $1\sigma$  RMS flux error (mJy) of the aperture photometry (column 5). Tab. 2 has the same structure except that we specify as flux the  $3\sigma$  upper limit. Notes to 3CR galaxies detected by ISOCAM are given in Appendix A.

In Fig. 1 we compare the radio flux and redshift distribution of 3CR sources detected with ISOCAM to galaxies of the parent catalogue. From the top panel of Fig. 1 it becomes evident that the fraction of 3CR galaxies detected in our survey is a strong function of radio flux, which spans two orders of magnitude. For example of the sources with an 178 MHz flux  $\lesssim 10$  Jy we detect only 15%, whereas for sources with an 178 MHz flux stronger than 30 Jy

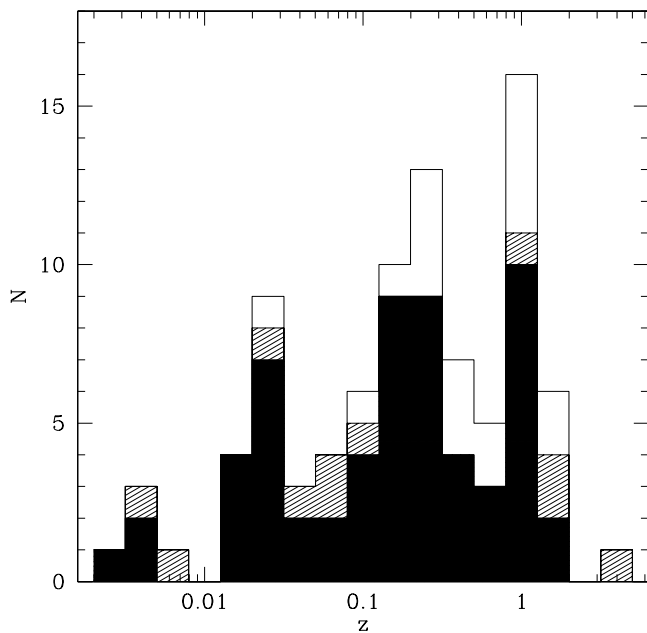


**Fig. 2.** Detection rate of 3CR sources in our survey as a function of redshift. The filled part part of the columns refers to 3CR sources detected with ISOCAM where the MIR emission can be attributed to dust (see Sect.4). The shaded part represents all ISOCAM detections of the 3CR catalogue and the upper (blank) histogram shows the redshift distribution of 3CR sources sampled by ISOCAM.

$\sim 50\%$  of all 3CR sources are detected. Furthermore, the galaxies detected with ISOCAM follow, by and large, the redshift–flux distribution of the parent catalogue (lower box of Fig. 1), at least, for redshifts larger than about 0.2. However, at  $z < 0.2$ , our subsample seems to show a preponderance of radio bright objects.

The fact that low redshift objects are preferentially included raises the question whether this is due to flux limits of our survey, i.e. whether the ISOCAM detection rate strongly drops as a function of redshift. This is investigated in Fig. 2, where we present the detection rate of our survey as a function of redshift. From Fig. 2 one can see that the detection rate of local objects ( $z < 0.1$ ) is close to 100%. For  $z > 0.2$ , and then almost independent of redshift up to  $z \sim 1$ , the detection rate is  $\sim 75\%$ . Therefore our survey is in this redshift range not limited by the sensitivity of ISOCAM. We conclude that the AGNs of our survey present a fair subsample of the 3CR catalogue for redshifts larger than 0.2.

### 3.2. Spectral energy distributions

For each detected 3CR source we compiled photometric measurements from optical to radio wavelengths. Our primary source of information was the NASA/IPAC Extragalactic Database (NED). In addition, we availed ourselves of the IRAS fluxes (re-processing raw data with

XSCANPI, see NASA/IPAC home page), the ISOPHOT fluxes (Fanti et al. 2000, Meisenheimer et al. 2001, Van Bemmell et al. 2001, Andreani et al. 2002, Spinoglio et al. 2002, Haas et al. 2004), mm/submm continuum data (Krügel et al. 1990, Gear et al. 1994, Steppe et al. 1988, Steppe et al. 1995, Best et al. 1998, Cimatti et al. 1998, Robson et al. 2001, Haas et al. 2004) and 1.4 GHz fluxes from the NRAO VLA Sky Survey (Condon et al. 1998). The resulting observed SEDs are shown in Fig. 3, together with additional information discussed below.

The MIR emission of our radio galaxies may come from synchrotron radiation of the AGNs, stars within the galaxies and dust emission. We assume that bremsstrahlung can be neglected. To identify a synchrotron component at ISOCAM wavelengths, we extrapolated radio core fluxes of the 3CR sources with a power law or, if that was not possible, we assumed a spectral slope as derived from global radio properties. The latter include the core emission (a few arcsecs in size) and the radio lobes which may extend several arcmin. The ISOCAM observations have a resolution of  $\sim 10''$  and are centered on the AGNs. Consequently, one has to use radio core fluxes (Giovannini et al. 1988; Hardcastle & Worrall 1999) to avoid an overestimate of the synchrotron component. When such core fluxes were not available, we adopted the core–to–total radio power correlation by Giovannini et al. (2001) to derive some estimate. As can be seen from Fig. 3, the synchrotron contribution to the MIR emission is generally small. One exception is the BL Lac 3C371, which will be neglected in the following.

We assess the significance of the stars by fitting a redshifted  $T = 4000\text{K}$  blackbody to the optical and near infrared data and extrapolate it to the MIR. The effective temperature was chosen deliberately low to maximise the effect of the stars at MIR wavelengths. The further interpretation of this curve depends on the size of the optical relative to the ISOCAM image. When they are comparable, we directly subtracted from the ISOCAM flux the extrapolated stellar flux. When the optical observation comprised a much larger region, the stellar component was considered as the upper limit of a stellar component within the ISOCAM aperture. The stellar component is simply added to the emission of the galaxy without any radiative transfer calculations. Indeed, for some of our sources the ISOCAM flux is dominated by stars from the host galaxy (see, for instance, the SED of 3C270 in Fig. 3). To quantify the likely contribution of the dust emission to the ISOCAM fluxes, we present below radiative transfer models of dust enshrouded AGNs.

## 4. Radiative transfer in dusty AGN

Here we outline an AGN dust model which is based on three free parameters. This simple model seems sufficient to fit the dust emission of the observed SED. After some motivation we present the model of the central engine and of the dust, the parameters and a library of reference SEDs. Then we discuss model properties and the fit to the

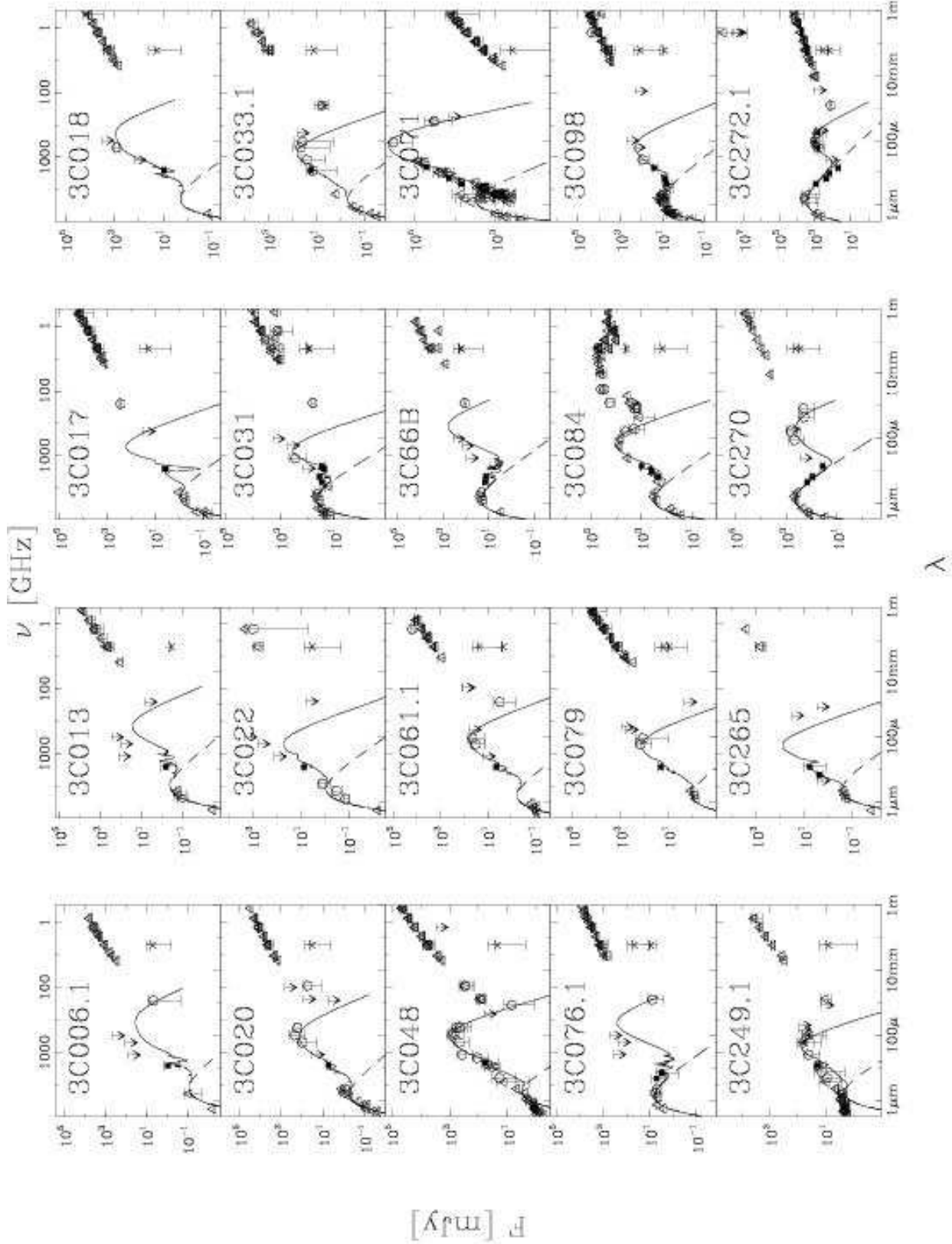


**Fig. 3.** Observed spectral energy distributions of the sources of the ISOCAM survey: ISOCAM photometry (filled squares), NED data (triangles), submillimeter data (pentagons), radio core fluxes (asterisks). Error bars are  $1\sigma$  and upper limits  $3\sigma$  RMS. Solid lines represent the addition of the photospheric component (dashed lines) and the dust emission resulting from the AGN models.

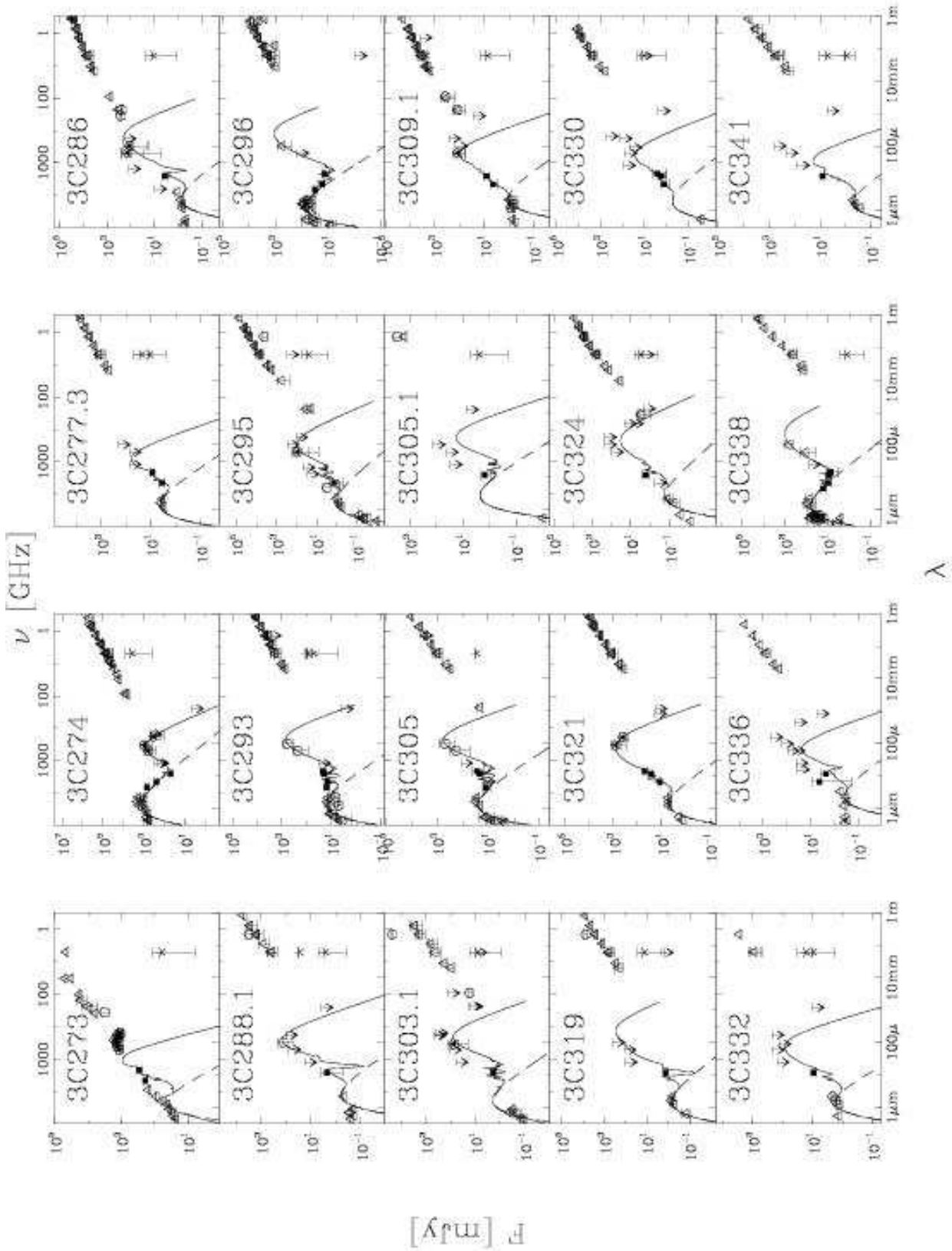


Fig. 3. – continued –

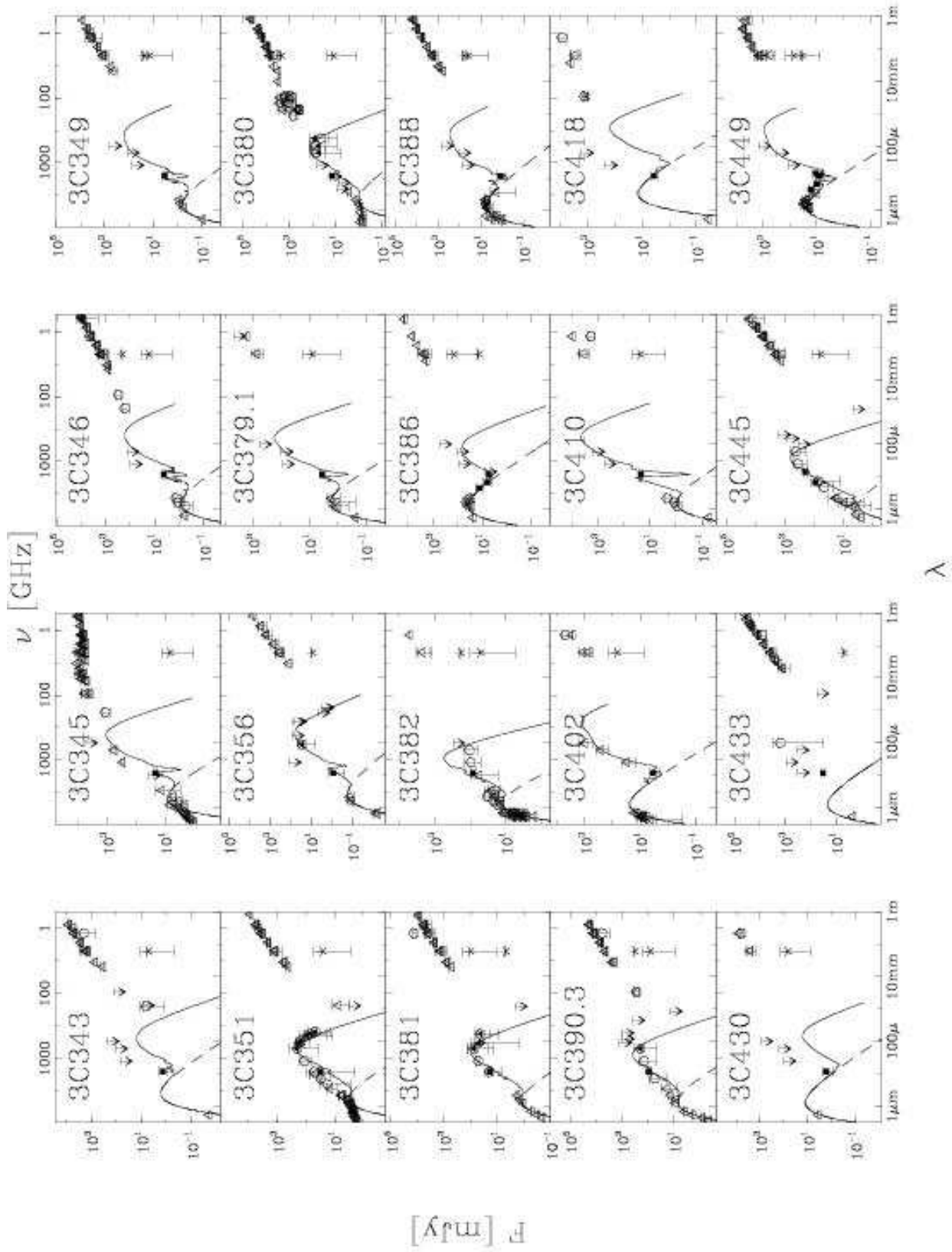


Fig. 3. – continued –

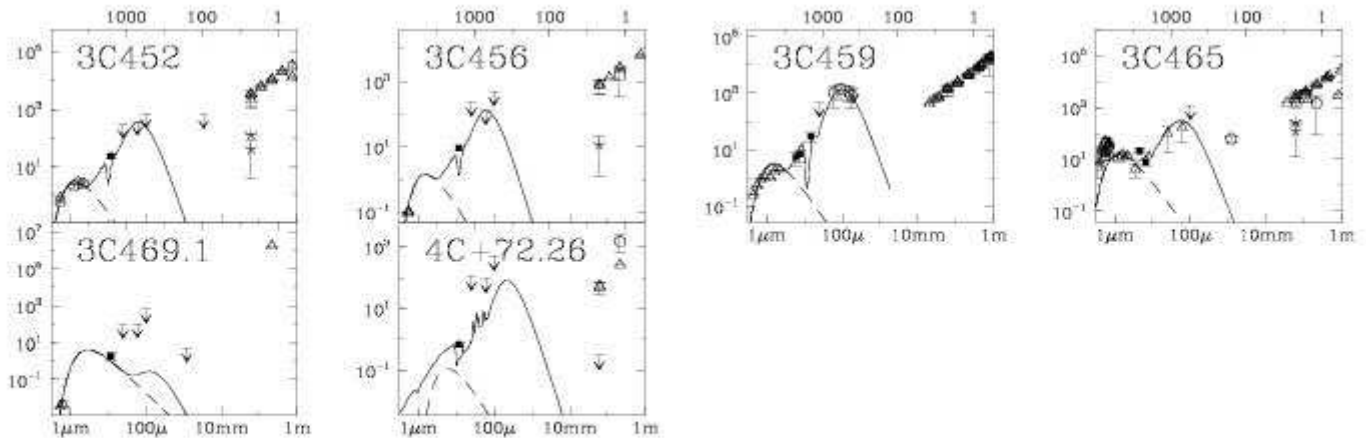


Fig. 3. – continued –

data. The computation of the dust emission together with the procedure to consider photospheric and synchrotron components provides a tool to specify a likelihood of the detection of dust in radio – loud AGN. Notes on fits of individual sources are given in Appendix B.

#### 4.1. Motivation

In most 3CR objects, the mid and far IR flux cannot arise from stars nor from the radio core because an extrapolation of either component to the infrared fails by orders of magnitude. This confirms the widely held view that the MIR/FIR emission of 3CR sources is often dominated by the dust (Meisenheimer et al. 2001, Van Bemmell et al. 2001, Andreani et al. 2002, Freudling et al. 2003, Haas et al. 2004). As the sources are not optically thin, one has to somehow compute the radiative transfer. In our procedure we self-consistently solve the radiative transfer in spherical symmetry with a ray-tracing method. The heating source of the dust is the central engine, scattering by dust is taken into account. Absorption and scattering efficiencies as well as asymmetry factors of the grains are calculated from Mie theory. The size distribution which the dust grains display is approximated by 8 different grain sizes for carbon and silicate material, respectively. Collisional heating (Contini & Contini 2003) is disregarded. The dust model includes a component of tiny and transiently heated particles. Further details can be found in Siebenmorgen et al. (1992). Observations pertaining to the distribution of dust in 3CR galaxies were performed by Martel et al. (1999) using the HST. Most galaxies could be resolved and dust was found close to the central heating source as well as far (few kpc) from it. Their images imply a complex morphology of the dust obscuration which defies any simple mathematical description. To be computational tractable, a radical simplification of the geometry is needed. As there are only few observational infrared data points for each galaxy, a sophisticated source structure that would require for its specifi-

cation more parameters than available data points is not warranted. We therefore consider spherical symmetry.

This is, of course, not in agreement with the unified scheme where the AGN is surrounded by an accreting disk or a torus and the phenomenological type is determined by the viewing angle of the observer. Such a configuration is intrinsically, at least, axisymmetric. However, the strongest effect brought about by the torus on the emerging spectrum occurs, of course, at visual and ultraviolet wavelengths. In the infrared, which we try to reproduce, the distance of the dust to the source and its mass are more important. Therefore, when barring the short wavelengths, a sphere can still conserve key elements of a multi-dimensional object. We note also that the angular (not the radial) distribution of the dust is in radiative transfer calculations only of importance when the source is opaque.

The dust distribution in the model is a spherical average over the true distribution. When applied to fitting an observed SED, such a model will tend to overestimate the near infrared emission of a type 2 AGN (edge-on viewed disk), and underestimate it for a type 1 (pole-on oriented disk). Nevertheless, as viewing angles cover a continuous range, in a statistical analysis, one should get about the right amount of cold and hot dust as well as an estimate of their distances from the central heating source.

Another reason to apply here spherically symmetric models stems from the well known difficulty which disks have in explaining the  $10\mu\text{m}$ -silicate band. This resonance lies in a spectral region covered by ISOCAM. When viewed face-on, disks should show the feature in emission, contrary to what is observed. Spherical models, on the other hand, are not heavily plagued by this problem as there is always some extinction towards the center. As a third argument we point out that for one of the best known AGNs, in the Circinus galaxy, a spherical model proves as efficient in reproducing the observed infrared SED and the wavelength dependence of the infrared sizes (Siebenmorgen et al. 1997) as do two-dimensional models (Ruiz et al. 2001).

The reason lies in the fact that most infrared data are of low spatial resolution.

Previous AGN torus models (e.g. Pier & Krolik 1993, Efstathiou & Rowan–Robinson 1995) do not include the dust in the host galaxy. Such models therefore miss the cold dust altogether. As the apertures of FIR observations are large one has to artificially include in these models a cold component (Farrah et al. 2003), whereas we incorporate it energetically self-consistent. Finally, the dust distribution as derived from HST images (de Koff et al. 2000) has so far never revealed a perfect torus like structure.

#### 4.2. The central engine

The central engine is approximated by a (small) sphere with a power law monochromatic luminosity  $L_\nu \propto \nu^{-0.7}$  in the range from  $10\text{\AA}$  to  $2\mu\text{m}$ . The exact lower limit,  $\lambda_{\text{low}}$ , should not be important as the dust becomes transparent (Dwek & Smith 1996). The upper limit,  $\lambda_{\text{up}}$ , is equally uncertain and represents a synchrotron break. Fortunately, the choice of  $\lambda_{\text{low}}$  and  $\lambda_{\text{up}}$  has little influence on the final IR spectrum.

#### 4.3. The dust model

The dust consists of large carbon and silicate grains with radii,  $a$ , between  $300$  and  $2400\text{\AA}$  and a size distribution  $n(a) \propto a^{-3.5}$ ; very small graphites ( $a = 10\text{\AA}$ ); and two kinds of PAHs (30 C and 20 H atoms; 252 C and 48 H atoms) which are responsible for various infrared emission bands (see Siebenmorgen et al. (2001) and Siebenmorgen et al. (2004) for details of the dust model).

The contribution of the different dust populations to the AGN spectrum is studied in Fig. 4. For fixed intrinsic luminosity of the AGN  $L = 10^{12} L_\odot$ , radius  $R = 1$  kpc and dust extinction  $A_V = 8$  mag we show the SED for three dust models: i) large grains only; ii) large grains and small graphites; iii) all dust components are included (large grains, small graphites and PAHs). Of particular interest for the interpretation of our ISOCAM observations is the MIR. Here dust emission below  $6\mu\text{m}$  is due to small graphites which become very hot ( $\gtrsim 1000$  K) after absorption of a single UV photon. The emission between  $6$  and  $9\mu\text{m}$  and near  $11.3$  and  $12.8\mu\text{m}$  is dominated by the PAH bands. Large grains with temperatures  $\sim 300$  K contribute to the emission at wavelengths  $\sim 10\mu\text{m}$ . At FIR/submm wavelengths, the emission is entirely due to cold large grains ( $\lesssim 50$  K). In summary the entire MIR is dominated by the emission of *hot dust* which may be either large grains heated to high temperatures, small graphites or PAH.

#### 4.4. Model library

In the spectra displayed in Fig. 3, one can usually make out three components: optical and near infrared emission, probably of stellar origin ( $\lesssim 5\mu\text{m}$ ), the mid and far infrared

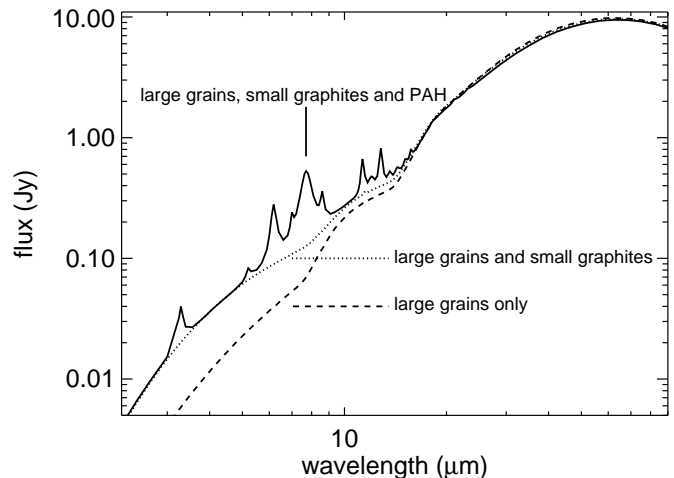


**Fig. 4.** The influence of the dust population on the infrared spectrum of the AGN. Model parameters are: visual extinction  $A_V = 8$  mag, radius  $R = 1$  kpc, luminosity  $L = 10^{12.5} L_\odot$  at distance of 50 Mpc. Model with large grains only (dashed), with large grains and small graphites (dotted), full model with large grains, small graphites and PAH (solid line).

( $5\mu\text{m} \lesssim \lambda \lesssim 1000\mu\text{m}$ ), and the radio regime ( $> 1000\mu\text{m}$ ). Our fits concern only the second component which we assume to be due to dust and to originate in the central, few kpc region of galactic nucleus. The optical and radio emission come from totally separated areas and may thus simply be added to the mid and far IR spectrum.

To keep the models and their subsequent interpretation as simple as possible, we consider only three basic parameters: the luminosity, the effective linear size of the galaxy, and the dust (or gas) mass. Furthermore, we adopt a constant dust density. We may then alternatively use as parameters: luminosity  $L$ , radius  $R$ , and visual extinction  $A_V$ .

We build a set of reference models<sup>1</sup> by varying  $L$ ,  $A_V$  and  $R$  in discrete steps over a wide range. In particular, we change the luminosity from  $10^{8.5}$  to  $10^{15.25} L_\odot$ , the visual extinction from 1 to 128 mag and the outer radius of the interstellar cloud that surrounds the AGN from 0.125 to 16 kpc; the inner radius of the dust shell is chosen to be close to the evaporation radius of the grains; a typically number is 1 pc.

#### 4.5. Model properties

In our models, the central engine of the AGN is the sole source for heating the dust. Alternatively, the dust could, at least partially, be heated by a starburst activity. The influence on the spectrum is investigated in Fig. 5 where we compare an AGN with a starburst model. In either

<sup>1</sup> The full set of models is available at: [http://eso.org/~rsiebenm/agn\\_models](http://eso.org/~rsiebenm/agn_models)

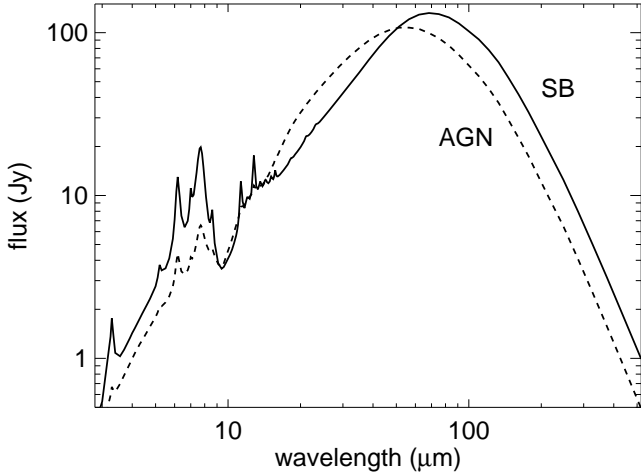


**Fig. 5.** Comparison of radiative transfer computations of dusty starbursts (solid) and AGNs (dashed). In both models we applied a visual extinction of  $A_V = 32$  mag, luminosity of  $L = 10^{12} L_\odot$  at distance of 50 Mpc, and radius of  $R = 1$  kpc.

model, the visual extinction  $A_V = 32$  mag, the luminosity  $L = 10^{12} L_\odot$  and the cloud radius is  $R = 1$  kpc. In the starburst, all stars have a uniform luminosity and temperature ( $L_* = 20000 L_\odot$ ,  $T_{\text{eff}} = 20000$  K) and are surrounded by a local dust shell of constant density  $10^4$  H-atoms/cm<sup>3</sup> (for details of the radiative transfer in a starburst, see Krügel & Siebenmorgen 1994). We see in Fig. 5 that in the SED of a starburst the PAH features and the submillimeter emission are considerably stronger. As our simple AGN model already fit observed spectra of radio-loud quasars (Freudling et al. 2003) we simplify our procedure and ignore in the following any starburst component.

Once we have chosen to use AGN models, there are three basic parameters in our modelling. The AGN luminosity of the models is in most cases well constrained by the data and corresponds to the integrated flux. The total extinction determines absorption features within the spectrum whereas the outer radius of the dust can be used to balance the relative amount of hot and cold dust for a given extinction.

The influence of the extinction,  $A_V$ , on the SED is shown in Fig. 6 for three different luminosities and for a fixed radius of 1 kpc. For the same luminosity and radius a high extinction implies strong submillimeter emission, a deep silicate absorption feature at  $10 \mu\text{m}$  and highly reddened radiation at shorter wavelengths. When the extinction is low, on the other hand, the AGN becomes optically visible, the silicate feature disappears and the submillimeter flux is weak. The SED peak may be used as a measure of the average dust temperature of the bulk material. For the same  $R$  and  $L$  value a lower  $A_V$  implies a SED peak at shorter wavelengths as compared to models with high  $A_V$ . On average, the dust is then much warmer. The bulk material becomes, of course, also warmer when the AGN

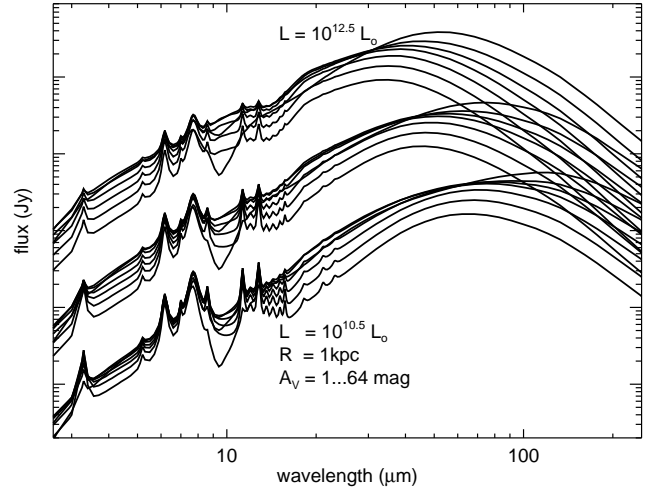


**Fig. 6.** AGN model spectra are shown for visual extinctions of  $A_V = 1, 2, 4, 8, 16, 32$  and  $64$  mag and luminosities of  $L = 10^{10.5}, 10^{11.5}$  and  $10^{12.5} L_\odot$  at a distance of 50 Mpc. The radius is fixed at  $R = 1$  kpc.

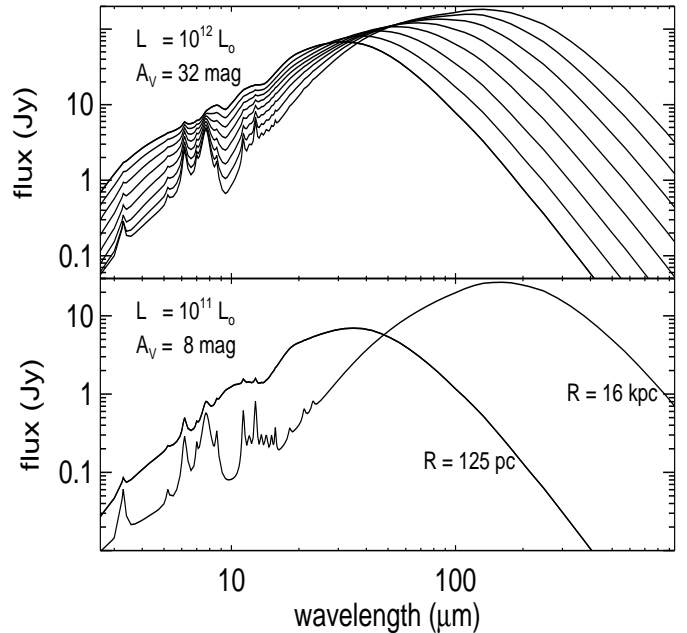


**Fig. 7.** The influence of the radius on the AGN model spectra. We apply a distance of 50 Mpc. Top: For luminosity of  $L = 10^{12} L_\odot$  and extinction of  $A_V = 32$  mag we present models with  $R = 0.125, 0.25, 0.5, 1, 2, 4, 8$  and  $16$  kpc. Bottom: For luminosity of  $L = 10^{11} L_\odot$  and extinction of  $A_V = 8$  mag we show models with  $R = 0.125$  and  $16$  kpc.

luminosity increases: models with same extinction and radius show a SED peak shifted to shorter wavelengths at higher luminosities (Fig. 6).

In Fig. 7 extinction and luminosity are held constant and the influence of the radius,  $R$ , on the SED is illus-

**Table 4.** Infrared dust luminosity of 3CR radio galaxies. Galaxies where spectral shape of the dust emission is constrained are marked in bold.

Name	z	Type	$\log(L_{\text{dust}})$ [ $L_{\odot}$ ]	R [pc]	$A_V$ [mag]	Dust ?
<b>3C006.1</b>	0.840	NLRG/FRII	11.75	16000	32	certain
3C013	1.351	NLRG/FRII	12.25	16000	2	likely
3C017	0.220	BLRG	11.5	125	128	likely
3C018	0.188	BLRG	12	16000	32	certain
<b>3C020</b>	0.174	NLRG/FRII	11.25	2000	16	certain
3C022	0.937	BLRG/FRII	12.5	500	8	possible
<b>3C031</b>	0.017	LERG/FRI	10	125	2	certain
<b>3C033.1</b>	0.181	BLRG/FRII	11.25	125	16	certain
<b>3C048</b>	0.367	QSO	12.75	4000	32	certain
<b>3C061.1</b>	0.186	NLRG/FRII	11	1000	16	certain
3C66B	0.212	LERG/FRI	9.75	16000	2	certain
<b>3C071</b>	0.004	NLRG	11.5	2000	16	certain
3C076.1	0.032	LERG/FRI	<9.75	16000	2	no evidence
<b>3C079</b>	0.256	NLRG/FRII	11.75	500	16	certain
<b>3C084</b>	0.018	NLRG/FRI	11.25	2000	4	certain
<b>3C098</b>	0.031	NLRG/FRII	10	125	32	certain
3C231	0.007	LERG/FRI	10.5	1000	16	certain
<b>3C249.1</b>	0.312	QSO	11.75	125	32	certain
3C265	0.811	NLRG/FRII	12.5	125	64	certain
3C270	0.007	NLRG/FRI	< 8.75	2000	32	no evidence
3C272.1	0.003	LERG/FRI	9	500	2	certain
3C273	0.158	QSO	12.75	500	1	possible
3C274	0.001	NLRG/FRI	< 9	250	2	no evidence
<b>3C277.3</b>	0.086	BLRG	10.5	250	1	certain
3C286	0.849	QSO/	12.5	8000	64	certain
3C288.1	0.961	QSO	12.5	1000	128	likely
<b>3C293</b>	0.045	LERG/FRI	10.75	8000	2	certain
3C295	0.461	NLRG/FRII	12.25	8000	1	certain
3C296	0.461	LERG/FRI	10	16000	8	likely
3C303.1	0.267	NLRG/FRII	11.5	16000	1	certain
<b>3C305</b>	0.041	NLRG/FRI	10.75	8000	1	certain
3C305.1	1.132	NLRG	< 12	8000	2	no evidence
<b>3C309.1</b>	0.905	QSO	12.75	250	32	certain
3C319	0.192	LERG/FRII	11.25	8000	128	likely
<b>3C321</b>	0.096	NLRG/FRII	11.5	2000	16	certain
<b>3C324</b>	1.206	NLRG/FRII	12.25	4000	8	certain
<b>3C330</b>	0.550	NLRG/FRII	11.75	125	32	certain
3C332	0.152	BLRG/FRII	11.25	16000	2	certain
3C336	0.927	QSO	12	250	4	certain
<b>3C338</b>	0.029	NLRG/FRI	10.25	16000	16	certain
3C341	0.448	NLRG/FRII	11.75	125	2	certain
3C343	0.988	QSO	11.75	2000	16	possible
3C345	0.593	QSO	13	16000	64	certain
3C346	0.161	NLRG/FRII	11	16000	16	likely
3C349	0.205	NLRG/FRII	11.25	16000	32	certain
<b>3C351</b>	0.372	QSO	12.25	500	32	certain
<b>3C356</b>	1.079	NLRG/FRII	12.25	4000	64	certain
3C371	0.051	BL Lac	< 11.5	16000	32	no evidence
3C379.1	0.256	RG	11.5	4000	64	certain
<b>3C380</b>	0.691	QSO	12.5	1000	32	certain
<b>3C381</b>	0.159	BLRG/FRII	11.25	250	32	certain
<b>3C382</b>	0.058	BLRG/FRII	11	125	2	certain

**Table 4.** continued

Name	z	Type	$\log(L_{\text{dust}})$ [ $L_{\odot}$ ]	$R$ [pc]	$A_V$ [mag]	Dust ?
3C386	0.017	LERG/FRI	9	125	16	possible
3C388	0.090	LERG/FRII	<10.75	8000	64	no evidence
<b>3C390.3</b>	0.056	BLRG/FRII	11	125	4	certain
3C402	0.023	NLRG	10	16000	128	certain
3C410	0.249	RG	12.75	16000	128	certain
3C418	1.686	QSO	< 8.5	16000	128	no evidence
3C430	0.054	NLRG	< 9	250	128	no evidence
3C442	0.026	LERG/FRI	< 8.5	16000	128	no evidence
<b>3C445</b>	0.056	BLRG/FRII	11.5	125	16	certain
3C449	0.017	BLRG	9.75	8000	64	possible
3C452	0.081	NLRG/FRII	11	250	64	certain
3C456	0.233	LERG	11.5	250	64	certain
<b>3C459</b>	0.200	NLRG/FRII	12.25	2000	128	certain
3C465	0.030	LERG/FRI	10.25	125	32	certain
3C469.1	1.336	LERG/FRII	< 8.5	16000	128	no evidence
4C+72.26	3.532	RG	13.5	250	64	no evidence

trated. We present models with high extinction  $A_V = 32$  mag and luminosity  $L = 10^{12} L_{\odot}$  as well as moderate extinction  $A_V = 8$  mag and luminosity  $L = 10^{11} L_{\odot}$ , respectively. When the radius is large, most of the dust is farther away from the AGN and therefore on average much cooler when compared to models with small  $R$ . When the radius of the model is increased while the extinction is kept fixed more dust is needed for the same submillimeter flux. As the luminosity is constant the MIR emission becomes fainter for models with large  $R$  and the SED peak is shifted to longer wavelengths.

Another important feature of the SED is the strength of the PAH emission. In Fig. 7 (bottom) one notices that PAH band emission increases for models with increasing cold dust, respectively large radii. If  $R$  is small the models predict more hot dust and relatively weak or fully absent PAH bands. This is because most of the dust emission originates nearby the central source and only few PAH survive the harsh AGN environment.

To constrain the models one needs MIR and FIR data. The FIR observations shall give a measure of the SED peak emission. We have studied the degeneration of our AGN models. As may be obvious, for sources where the FIR peak is reasonably well known but there is only a single data point in the MIR it is still possible to fit the SED by a combination of low extinction and large radius or vice versa. However, when more MIR data are available the degeneration almost disappears. In particular for galaxies where the ISOCAM data are suited to indicate the depth of the silicate band the models are quite unique. This is because the depth of the silicate absorption is directly related to the visual extinction.

#### 4.6. Fit to Data

We selected models from the AGN library (see Sect. 4.4) which are consistent with the data. First we require that the models smoothed to the ISOCAM bandwidths predict the measured ISOCAM fluxes to within 10% accuracy. Second, we rejected models which violate any  $3\sigma$  upper limit. Of the remaining models, we choose the ones which best fit the optical to FIR/submillimeter data in a least square sense. The optical data can be reasonably approximated by a blackbody of a few thousand K. We therefore assume that they are due to (weakly reddened) stars and this stellar component is fit separately. As a result one obtains the stellar luminosity (see Fig. 8). In 16 out of 69 cases the  $A_V$  of the model is  $\lesssim 2$  mag and then the AGN may also contribute at optical wavelengths. The model flux (AGN) is then subtracted from the measured flux and only the rest is used to evaluate the luminosity of the stars. The models are shown as solid lines in Fig. 3. They fit generally well, exceptions are: 3C273, or 3C382 (see Appendix B for notes on individual fits).

The results of our modelling procedure are summarised in Tab. 4. We specify the name, redshift (as available in NED), type (Veron-Cetty & Veron 2000, Spinrad et al. 1985), infrared dust luminosity (Sect. 4) and specify a likelihood of dust detection. We distinguish four cases:

- *No evidence* for dust emission is found. ISOCAM and other flux measurements are consistent with a photospheric or synchrotron component.
- Detection of dust emission is *possible*. ISOCAM photometry is only slightly above the photospheric component and there are only far infrared data close to their detection or confusion limit.
- Detection of dust emission is *likely*. Here ISOCAM data are well above the predicted photospheric compo-

ment but there is a possible synchrotron contribution. There are no firm far infrared detections.

- Detection of dust emission is *certain*. There are reliable infrared detections well above the predicted photospheric component and the contribution by synchrotron or free-free emission can be ruled out.

## 5. Discussion

### 5.1. Energy budget: nucleus versus host

First, we compare how the AGN and the stars of the host galaxy contribute to the dust heating. The influence of a central starburst is not considered. One of the three basic parameters of each SED model is the AGN luminosity. In our spherical models, which are all optically thick ( $A_V \gtrsim 1$ ), the AGN luminosity is entirely re-radiated by dust in the infrared and it is denoted  $L_{\text{dust}}$ . The upper panel of Fig. 8 shows the AGN luminosity of all galaxies detected by ISOCAM as a function of redshift. In the lower panel, we divided  $L_{\text{dust}}$  by the luminosity of all the stars,  $L_{\text{star}}$ , in the galaxy. The latter was estimated from the black-body fits of the photospheric component displayed in Fig. 3 and are not de-reddened.

One notes a trend of  $L_{\text{dust}}$  with  $z$  which is typical for flux limited samples. As demonstrated in the lower panel of Fig. 8, the AGN luminosity is much higher than the stellar luminosity,  $L_{\text{star}}$ , which is concentrated in the near infrared and optical region. The powerful AGN heats the dust not only in its vicinity but throughout the galaxy and acceptable model fits to the observed SEDs were possible only when dust at large (several kpc) distances was included.

### 5.2. Dust emission and AGN unification

For 27 AGNs of our sample, marked bold face in Tab. 4, there exist enough photometric data to constrain the spectral shape of the dust emission. For a more detailed comparison, we distinguish between galaxies of optical spectral type 1 and 2 and between objects of high ( $L > 10^{11} L_{\odot}$ ) and low ( $L \leq 10^{11} L_{\odot}$ ) luminosity  $L$ . Altogether we thus have four classes: 6 BLRGs (type 1), 5 QSOs (type 1), 6 low  $L$  and 10 high  $L$  NLRGs (both of type 2). According to the unification scheme, type 1 AGNs are viewed nearly pole-on and have visible broad line region, whereas type 2 AGNs are viewed edge-on, so that the large extinction from the AGN torus obscures the broad-line region.

In Fig.9, we plot for the 27 objects the best fit parameters: radius and visual extinction. AGNs of type 1 occupy the left and those of type 2 the right part of the frame, so the models for them differ foremost by the size parameter or radius  $R$ . This was already evident from the infrared SEDs in Fig. 7 (bottom) where small model radii correspond to BLRGs and large radii to low luminosity NLRGs. For low luminosities, both NLRGs and BLRGs are fit by moderate extinction ( $\overline{A_V} \sim 7$  mag). For high lu-

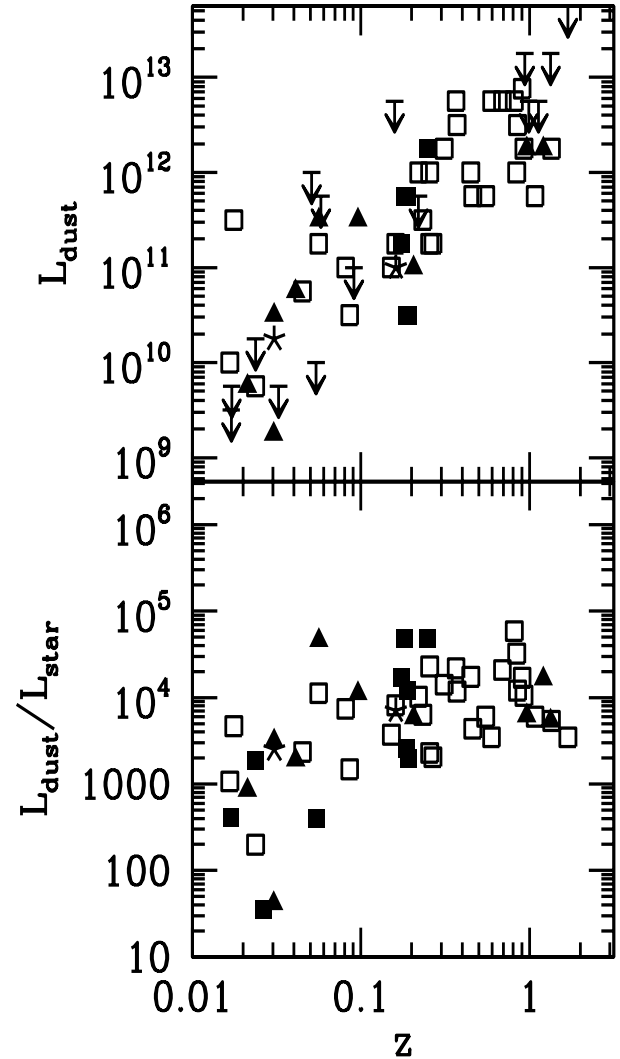


**Fig. 8.** Top: The intrinsic AGN luminosity of the model,  $L_{\text{dust}}$ , as function of redshift. Solid symbols are type 1 AGNs: triangles QSOs and squares BLRGs. Open squares are NLRGs and upper limits as of Tab. 4. Bottom: Luminosity ratio of AGN and stellar components as a function of redshift. Symbols as in top panel.

minosity NLRGs and QSOs, we find higher values of  $A_V$ , the averages are  $\overline{A_V} = 20$  and 30 mag, respectively. This trend is reflected for QSOs and high luminosity NLRGs in the top panel of Fig. 7, where SEDs with a radius close to the mean value of both AGN types can be compared.

In summary, the model spectra of BLRGs and QSOs (Fig. 7, bottom) peak at  $\sim 40 \mu\text{m}$ , whereas high and low luminosity NLRGs attain their maxima much longer wavelengths, around  $150 \mu\text{m}$ . Therefore, the dust in AGNs of type 1 is warmer than in those of type 2. This difference is qualitatively consistent with the unification schemes. For type 1 AGNs, which are viewed close to pole-on, the broad-line region is visible and unobscured hot dust dominates the SED. By contrast, towards NLRG, which are

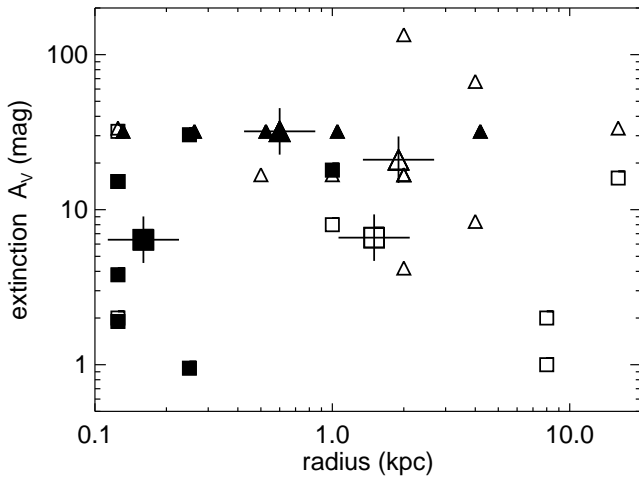


**Fig. 9.** The best fit model parameters, radius and dust extinction, for 27 galaxies with well determined SEDs. The objects are grouped according to their luminosity (high or low) and spectral type (1 or 2). There are QSOs (type 1, high  $L$ , filled triangles), BLRGs (type 1, low  $L$ , filled squares), NLRGs (type 2, high  $L$ , open triangles) and NLRGs (type 2, low  $L$ , open squares). For each type, log-arithmetic means are marked by crosses.

viewed face-on, large extinction from the torus obscures the broad-line region and pre-dominantly cooler dust is detected. The type 1 AGNs also show much less PAH emission than type 2. The weakness of the band emission in type 1, compared to type 2, is probably due to PAH destruction. Averages of observed SED are presented by Freudling et al. (2003) confirming the trends indicated in the models presented here.

## 6. Conclusions

ISOCAM detected 80% (71 out of 88) 3CR sources. We find evidence of hot dust in 53 radio galaxies or 75% of the sources detected in our survey. For each detected source, we compiled photometry from optical to radio wavelengths.

The extrapolation of radio core fluxes to ISOCAM wavelengths shows that synchrotron emission from the core is usually negligible in the MIR, exceptions being flat spectrum radio sources. The contribution of the host galaxy to the MIR is also generally small, here exceptions are a few sources of type FRI. Thus for most objects the origin of the MIR can be attributed mainly to dust. This dust is hot and heated by the central engine. The emission comes from large grains with temperatures of a few hundred Kelvin and small grains and PAHs undergoing temperature fluctuations. This picture is supported by simple radiative transfer calculations. Most SEDs can be successfully fit between 1 and  $1000\mu\text{m}$  by a three parameter model where AGN luminosity, size of the galaxy and extinction are varied. Our modelling shows that the

broad band data are consistent with AGN only heating of the dust.

For similar luminosities, we compare AGNs of type 1 and 2. We find that the model parameters depend strongly on the AGN type and a dichotomy of the infrared SEDs is derived. The IR fluxes of BLRGs and QSOs peak around  $40\mu\text{m}$  while the maximum of the dust emission for NLRGs is reached at  $\gtrsim 100\mu\text{m}$ . Therefore, the dust in type 1 AGNs is warmer than in type 2. The models also predict much weaker PAH emission in type 1 AGNs than in type 2, as a result of evaporation. Unfortunately, PAH bands cannot be resolved by the broad-band ISOCAM observations.

AGNs and starbursts are accompanied by tremendous IR luminosities. Although the possible coexistence of both energy sources and their relative contributions to the dust heating is difficult to assess, starbursts tend to favour PAH emission and this may serve as a possible discriminator of activity.

*Acknowledgements.* We thank the referee, Cristina Popescu, for constructive and detailed suggestions. Rosario Lorente at the ISO Data Centre for archiving support. Martin Haas thanks for grants from the Nordrhein-Westfälische Akademie der Wissenschaften, funded by the Federal State Nordrhein-Westfalen and the Federal Republic of Germany. This research has made use of the SIMBAD database, operated at CDS, Strasbourg, France and the NASA/IPAC Infrared Science Archive and Extragalactic Database (NED) which is operated by the Jet Propulsion Laboratory, California Institute of Technology, under contract with the National Aeronautics and Space Administration. This publication makes use of data products from the Two Micron All Sky Survey, which is a joint project of the University of Massachusetts and the Infrared Processing and Analysis Center/California Institute of Technology, funded by the National Aeronautics and Space Administration and the National Science Foundation. CIA is a joint development by the ESA Astrophysics Division and the ISOCAM Consortium. The ISOCAM Consortium is led by the ISOCAM PI, C. Cesarsky.

## References

- Andreani P., Fosbury R. A. E., van Bemmell I., Freudling, W., 2002, *A&A* 381, 389
- Akujor C.E., Ludke E., Browne I.W.A., Leahy J.P., Garrington S.T., et al., 1994, *A&A* 105,247
- Akujor C.E., Garrington S. T., 1995, *A&AS* 112, 235
- Axon D.J., Capetti A., Fanti R., Morganti R., 2000, *AJ* 120, 2284
- Barthel P.D., 1999, *ApJ* 336, 606
- Baum S.A., O’Dea C.P., Giovannini G., Biretta J., Cotton, W.B., et al. , 1997, *ApJ* 483, 178
- Best P.N., Röttgering H.J.A., Bremer M.N., et al., 1998, *MNRAS* 301, L15
- Best P.N., Longair M.S., Röttgering H.J.A., 1998, *MNRAS* 295, 549
- Blommaert J., Siebenmorgen R., Coulais A., et al., 2001, “ISO Handbook Volume III (CAM)”, SAI-99-057/Dc, <http://www.iso.vilspa.esa.es>
- Boisse P., Le Brun V., Bergeron J., Deharveng J.-M., 1998, *A&A* 333, 841

- Brunetti G., Setti G., Comastri A, 1997, *A&A* 325, 898
- Canalizo G., Stockton A., 2000, *ApJ* 528, 201
- Capetti A., De Ruitter H.R., Fanti R., et al., 2000, *A&A* 362, 871
- Cesarsky C., Abergel A., Agnèsè P. et al., 1996, *A&A* 315, L32
- Cimatti A., Freudling W., Rottgering H.J.A., Ivison R.J., Mazzei P., 1998, *A&A* 329, 399
- Chambers K.C., Miley G.K., van Breugel W.J.M., Huang J.-S., Trentham A., 1996, *ApJS* 106, 247
- Colbert J.W., Mulchaey J.S., Zabludoff A.I., 2001, *AJ* 121, 808
- Condon, W. D., Greisen E.W., Yin Q.F., Perley R.A., et al., 1998, *AJ* 115, 1693
- Contini M., Contini T., 2003, *MNRAS* 342, 299
- Coulais A., Abergel A., 2000, *A&AS* 141, 533
- Crawford C.S., Fabian A.C., 1996, *MNRAS* 281, 5
- de Koff S., Baum S.A., Sparks W.B., Golombek D., Biretta J., et al., 1996, *ApJS* 107, 621
- de Koff S., Best P., Baum S.A., Sparks W., Rottgering H., et al., 2000, *ApJS* 129, 33
- de Juan L., Colina L., Golombek D., 1996, *A&A* 305, 776
- de Vaucouleurs G., de Vaucouleurs A., Corwin H.G., 1976, *Second reference catalogue of bright galaxies*, Austin University of Texas, Press.
- de Vries W.H., O’Dea C.P., Baum S.A., Sparks W.B., Biretta J., 1997, *ApJS* 110, 191
- Djorgovski S., Spinrad H., McCarthy P., Dickinson M., van Breugel W., et al., 1988, *AJ* 96, 836
- Draper P.W., Scarrott S.M., Tadhunter C.N., 1993, *MNRAS* 262, 1029
- Dwek E., Smith R.K., 1996, *ApJ* 459, 686
- Efstathiou A., Rowan–Robinson, 1995, *MNRAS* 273, 649
- Eracleous M., Halpern J.P., 1994, *ApJS* 90, 1
- Fanti C., Pozzi F., Fanti R., et al., 2000, *A&A* 358, 499
- Farrah D., Afonso J., Efstathiou, A., et al., 2003, *MNRAS* 343, 585
- Fernini I, Burns J.O., Bridle A.H., Perley R.A., 1993, *AJ* 105, 1690
- Ford H. C., Tsvetanov Z. I., Kriss G. A., Harms R., Dressel L., 1994, *A&AS* 184, 6402
- Freudling W., Siebenmorgen R., Haas M., 2003, *ApJL* 599, 13
- Gear W.K., Stevens J.A., Hughes D.H., et al. 1994, *MNRAS* 267, 167
- Giovannini G., Feretti L., Gregorini L., Parma P., 1998, *A&A* 199, 73
- Giovannini G., Cotton W.D., Feretti L., Lara L., Venturi T., 2001, *ApJ* 552, 508
- Granato G.L., Danese L., 1994, *MNRAS* 268, 235
- Hardcastle M.J., Worrall D.M., 1999, *MNRAS* 309, 969
- Haas M., Müller S. A. H., Bertoldi F., et al., 2004, *A&A* submitted
- Harms R., Ford H., Tsvetanov Z. I., et al., 1994, *ApJ* 435, 35
- Harvanek M., Hardcastle M.J., 1998, *ApJS* 119, 25
- Heckman T.M., O’Dea C.P., Baum S.A., and Laurikainen E. 1994, *ApJ* 428, 65
- Jackson N., Rawlings S. 1997, *MNRAS* 286, 241
- Jackson N., Beswick R.J., Pedlar A., et al., 2003, *MNRAS* 338, 643
- Jaffe W., Ford H., Ferrarese L., van den Bosch F., O’Connell R. W., 1996, *ApJ* 460, 214
- Katajainen S., Takalo L. O., Sillanpää A., 2000 *A&AS*, 143, 357
- Kotanyi C.G., Ekers R.D., 1979, *A&A* 73, L1
- Krügel E., Chini R., Klein U., et al., 1990, *A&A* 240, 232
- Krügel E., Siebenmorgen R., 1994, *A&A* 288, 929
- Laing R.A., Jenkins C.R., Wall J.V., Unger S.W., 1994, *The First Stromlo Symposium: The Physics of Active Galaxies*. ASP Conference Series, Vol. 54, 1994, G.V., 201
- Leahy J.P., Perley R.A., 1991, *AJ* 102, 537
- Leech K., Pollock A.M.T., 2001, “ISO Handbok Vol. II”, SAI-99-082/Dc, <http://www.iso.vilspa.esa.es>
- Lehnert M.D., Miley G.K., Sparks W.B., Baum S.A., Biretta J., 1999, *ApJS* 123, 351
- Leon S., Lim J., Combes F., Van-Trung D., 2001, *astro-ph/0107498*
- Laor A., Draine B.T., 1993, *ApJ* 402, 441
- Ludke E., Garrington S.T., Spencer R.E., Akujor C.E., Muxlow T. W. B., 1998, *MNRAS* 299, 467
- Martel A.R., Braun. S.A., Sparks W.B., Wyckoff E., Biretta J.A., et al., 1999, *ApJS* 122, 81
- McCarthy P. J., Spinrad H., van Breugel, W, 1995, *ApJS* 99, 27
- McCarthy P. J., Baum S.A., Spinrad H., 1996, *ApJS* 106, 281
- McCarthy P. J., Miley G.K., de Koff, et al., 1997, *ApJS* 112, 415
- Meisenheimer K., Haas M., Müller S. A. H., et al., 2001, *A&A* 372, 719
- Miller J.S., 1981, *PASP* 93, 681
- Morabito D.D., Preston R.A., Slade M.A., Jauncey D.L., 1982, *AJ* 87, 1639
- Nenkova M., Ivezić Z., Elitzur M., 2002, *ApJ* 355, 456
- Neugebauer G., Green R. F., Matthews K., Schmidt M., Soifer B. T., et al., 1987, *ApJS* 63, 615
- O’Dea P., de Vries W., Biretta J.A., Baum S.A., 1999, *AJ* 117, 1143
- Okumura K., ISOCAM PSF Report, 1998. [http://www.iso.vilspa.esa.es/users/expl\\_lib/CAM\\_list.html](http://www.iso.vilspa.esa.es/users/expl_lib/CAM_list.html)
- Ott S., Abergel A., Altieri B., et al., 1996, *ASAP Conference series*, Vol. 125, 1997
- Ott S., Pollock A., Siebenmorgen R., 2000, “The ISOCAM Parallel Mode”, *Proc. of a Ringberg Workshop, ISO Surveys of a Dusty Universe*, eds: D. Lemke, W. Stichel, K. Wilke, *Lecture Notes in Physics*, Springer (ISBN 3-540-67479-9), p. 289
- Peng B., Kraus A., Kirchbaum T.P., Witzel A., 2000, *A&AS*, 145, 1
- Penston M.V., Cannon R.O., 1970, *R. Obs. Bull.* 159, 85
- Pier A. P., Krolik J.H., 1993, *ApJ* 418, 673
- Popescu C.C., Tuffs R.J., Kylafis N.D., Madore B.F., 2004, *A&A* 414, 45
- Rantakyro F.T., Baath L.B., Backer D.C., et al., 1998, *A&AS* 131,
- Ridgway S.E., Stockton A., 1997, *AJ* 114, 511.
- Robson E.I., Stevens J.A., Jenness T., 2001, *MNRAS* 327, 751
- Roche N., Eales S.A., 1999, *MNRAS* 317, 120
- Roettgering H.J.A., Lacy M., Miley G. K., Chambers K. C., Saunders R.R, 1994, *A&AS* 108, 79
- Roman P., Ott S., 1999, Report on the behaviour of ISOCAM LW darks, ESA Technical Report, [http://www.iso.vilspa.esa.es/users/expl\\_lib/CAM\\_list.html](http://www.iso.vilspa.esa.es/users/expl_lib/CAM_list.html)
- Rowan–Robinson M., 2000, *MNRAS* 316, 885
- Schmidt M., 1963, *Nature* 197, 1040
- Siebenmorgen R., Krügel E., Mathis J.S., 1992, *A&A* 266, 501
- Siebenmorgen R., Moorwood A., Freudling W., Käuff H.U., 1997, *A&A* 325, 450.
- Siebenmorgen R., Krügel E., Laureijs R., 2001, *A&A* 377, 735
- Siebenmorgen R., Krügel E., Spoon H.W.W., 2004, *A&A* 414, 123

Siebert J., Matsuoka M., Brinkmann W., Cappi M., Mihara T., et al., 1996, *A&A* 307, 8  
 Simpson C., Rawlings S., Lacy M., 1999, *MNRAS* 306, 828  
 Spinoglio L., Andreani P., Malkan M. A., 2002, *ApJ* 572, 105  
 Spinrad H., Djorgovski S., Marr J., Aguilar L., 1985, *PASP* 97, 932  
 Starck, J.L., Siebenmorgen, R. & Gredel, R., 1997, *ApJ* 482, 1011-1020.  
 Starck J.L, Abergel A., Aussel H., Sauvage M., Gstaude R., et al., 1999, *A&AAS* 134, 135-148.  
 Steppe H., Salter C. J., Chini R., et al., 1988, *A&AS* 75, 317  
 Steppe H., Jeyakumar S., Saikia D. J., Salter C. J., 1995, *A&AS* 113, 409  
 Sudou H., Iguchi S., Murata Y., Taniguchi Y., 2003, *Science* 300, 1263  
 Worrall D. M., Birkinshaw M., 2000, *ApJ* 530, 719  
 Tadhunter C.N, Morganti R., di Serego Alighieri S., Fosbury R. A. E., Danziger I.J., 1993, *MNRAS* 263, 999  
 Taylor G. L., Dunlop J. S., Hughes D. H., Robson E. I., 1996, *MNRAS* 283, 930  
 Urry, C. M., Padovani P., 1995, *PASP* 107, 803  
 Van Bemmel I.M., Barthel P.D., de Graauw T., 2001, *A&A* 368, 414  
 Veron-Cetty M.-P., Veron, P., 2000, *A Catalogue of quasars and active nuclei*, 9th edition, published by ESO, [http://www.iso.vilspa.esa.es/users/expl\\_lib/CAM\\_list.html](http://www.iso.vilspa.esa.es/users/expl_lib/CAM_list.html)  
 Xu C., Baum S.A., O’Dea C., Wrobel J.M., Condon J.J., 2000, *AJ* 120, 2950  
 Yee H.K.C., Oke J.B., 1978, *ApJ* 226, 753  
 Zirbel E.L., Baum S. A., 1998, *ApJS* 114, 177

## Appendix A: Notes on individual galaxies

Our remarks below concern the following points: (1) previous indications of dust, (2) X-ray emission, (3) jets, (4) high excitation line emission, (5) morphology, (6) companions.

*3C002* ( $z = 1.037$ ): Fuzzy optical structure similar to radio morphology (Ridgway & Stockton 1997).

*3C006.1* ( $z = 0.804$ ): There is an optical extension with position angle roughly equal to that of the radio axis (McCarthy et al. 1997).

*3C013* ( $z = 1.351$ ): There are two faint tail-like structures to the south and east of the nucleus. The core radio source is a double with a size of  $28''$ .

*3C017* ( $z = 0.2$ ): X-ray source (Siebert et al. 1996) with a strong and broad H $\alpha$  line (Eracleous & Halpern 1994).

*3C018* ( $z = 0.19$ ): Shows a rich emission line spectrum with extremely high ionization states (Tadhunter et al. 1993).

*3C020* ( $z = 0.17$ ): Two cones of emission and a possibly dust disk are detected by de Koff et al. (2000). The large-scale FR II class radio structure is aligned roughly perpendicular to the proposed dust lane.

*3C022* ( $z = 0.935$ ): From JKL’ images. Simpson et al. (1999) conclude that 80% of the light in a  $3''$  aperture is from a weakly reddened ( $A_V = 2 - 5$ mag) quasar; extended near IR light is presumably photospheric.

*3C031* ( $z = 0.0167$ ): Associated with NGC383. HST images show a face-on dust disk with a diameter of  $7''$  and an unresolved core (Xu et al. 2000). Martel et al. (1999) confirm an optical synchrotron jet. The molecular gas content is  $M(\text{H}_2) \sim 10^9 M_\odot$  (Leon et al. 2001).

*3C33.1* ( $z = 0.181$ ): Broad line radio galaxy in a region of high foreground stellar density (McCarthy et al. 1995). A star is superimposed southeast of the nucleus.

*3C048* ( $z = 0.367$ ): Significant part of the OIII line emission is confined to the  $0.5''$  central region (Axon et al. 2000).

*3C61.1* ( $z = 0.186$ ): Narrow-line galaxy.

*3C66B* ( $z = 0.0212$ ): HST observations confirm an optical synchrotron jet (Martel et al. 1999). Orbital motion in this radio galaxy provides evidence for a supermassive black hole binary (Sudou et al 2003).

*3C071* (NGC1068,  $z = 0.003$ ): Famous Seyfert 2; MIR images of high spatial resolution are obtained by Siebenmorgen et al. (2004).

*3C076.1* ( $z = 0.0325$ ): A galaxy with no optical or near IR features (Colbert et al. 2001).

*3C079* ( $z = 0.256$ ): Narrow H $\alpha$  and H $\beta$  lines (Laing et al. 1994).

*3C083.1* (NGC1265,  $z = 0.025$ ): Edge-on radio galaxy with radio jet and nearly orthogonal narrow dust lane of  $\sim 1.5$  kpc. There is a bright foreground star near the center (Martel et al. 1999).

*3C084* (NGC1275,  $z = 0.0176$ ): Extensively studied giant elliptical galaxy. It has filamentary dust structures which extend out to 17 kpc (de Koff et al. 2000).

*3C098* ( $z = 0.031$ ): Seyfert 2 with extended X-ray emission and a compact central X-ray source (Hardcastle & Worrall 1999). No optical/near IR features (Colbert et al. 2001).

*3C231* (M82,  $z = 0.001$ ): Archetype starburst galaxy; see Krügel & Siebenmorgen (1994) for a model of the dust emission.

*3C249.1* (PG 1100+772,  $z = 0.312$ ): Absorption line quasar.

*3C264* ( $z = 0.022$ ): An apparent optical “ring” is claimed to be produced by a circumnuclear dust disk (Baum et al. 1997).

*3C265* ( $z = 0.811$ ): Complex optical structure without a point source at the nucleus. Probably highly obscured AGN ( $A_V \geq 15$ mag, Simpson et al. 1999).

*3C270* (NGC4261,  $z = 0.007$ ): Quasar with nuclear dust disk perpendicular to the large-scale radio jets (Jaffe et al. 1996). Indication of vigorous star formation around the AGN (Canalizo & Stockton 2000). The quasar suffers little extinction (Leon et al. 2001).

*3C272.1* (M84,  $z = 0.004$ ): Elliptical galaxy with dust extending out to almost 1 kpc (de Koff et al. 2000).

*3C273* ( $z = 0.158$ ): First discovered QSO (Schmidt 1963).

*3C274* (M87, NGC4486,  $z = 0.004$ ): It has an ionized disk surrounding the central black hole (Ford et al. 1994, Harms et al. (1994) of  $2.6 \cdot 10^9 M_\odot$  (Lauer et al. 1992).

*3C277.3* (Coma A,  $z = 0.086$ ): Elliptical with radio jet.

*3C286* ( $z = 0.849$ ): Contains high excitation line emission (Boisse et al. 1998).

*3C288.1* ( $z = 0.961$ ): Double radio quasar (Akujor et al. 1994).

*3C293* (UGC 08782,  $z = 0.045$ ): Has a double nuclei core with a steep radio spectrum and filamentary dust lanes (Martel et al. 1999).

*3C295* ( $z = 0.464$ ): Extended double-lobe radio galaxy without a core (Akujor et al. 1994, Fomalont et al. 2000).

*3C296* (NGC5532,  $z = 0.0237$ ): This elliptical galaxy hosts a sub-kiloparsec, elongated and sharp dusty structure centered on its nucleus (Martel et al. 1999).

*3C303.1* ( $z = 0.267$ ): The nucleus has an elongated shape. The extended radio source is an asymmetric double  $\sim 1.8''$  in size, elongated perpendicular to two dust lanes (de Koff et al. 2000).

*3C305* ( $z = 0.039$ ): An inclined disc of gas and dust encircling a quasar reddened by  $A_V > 4$  has been observed by Jackson et al. (2003).

*3C305.1* ( $z = 1.132$ ): The NED coordinates have an uncertainty of  $4''$ . In the DSS, a contaminating source is visible  $8''$  away. The radio emission of this high-redshift galaxy forms a core-free structure with two lobes separated by  $\sim 2''$ .

*3C309.1* ([HB89] 1458+718,  $z = 0.905$ ): This quasar has a compact steep radio spectrum (Peng et al. 2000) and remains unresolved in the optical (de Vries et al. 1997).

*3C319* ( $z = 0.192$ ): Resembles a normal non-star-forming elliptical with an optical long axis almost perpendicular to the radio axis (Roche & Eales 2000).

*3C321* ( $z = 0.096$ ): Blue, high surface brightness galaxy. The disturbed dust lane with a projected length of  $\sim 3.7''$  breaks in two components belonging to two merging galaxies (Roche & Eales 2000).

*3C324* ( $z = 1.206$ ): A gravitationally-lensed, extremely elongated high redshift radio galaxy (Chambers et al. 1996) with a steep radio spectrum ( $\alpha \sim 1.07$ , Brunetti et al. 1997). It is a ROSAT source with an X-ray luminosity of  $4.4 \times 10^{40} L_{\odot}$  (Hardcastle & Worrall 1999). From SCUBA and Effelsberg observations Best et al. (1998) conclude that the submillimeter signal is not associated with synchrotron emission.

*3C330* ( $z = 0.550$ ): Optically very luminous and relatively blue galaxy. The disk structure is dominated by line emission (McCarthy et al. 1996).

*3C332* ( $z = 0.152$ ): This broad line radio galaxy shows in HST images a smooth elliptical nuclear region (Taylor et al. 1996).

*3C336* (PKS 1622+23,  $z = 0.927$ ): This source has a large angular radio size ( $28''$ ). The brightest ISOCAM pixel is close to the radio source FIRST J162438.8+234505. The latter may be a resolved component of PKS 1622+23.

*3C338* (NGC6166,  $z = 0.030$ ): Elliptical in the cluster Abell 2199. An arc-like dust feature extends for  $\sim 3''$  from the nucleus to the West (Capetti et al. 2000).

*3C341* ( $z = 0.448$ ): As the NED coordinates are uncertain by  $3''$ , we use coordinates derived from DSS2. Martel et al. (1999) confirm an optical synchrotron jet.

*3C343* ( $z = 0.988$ ): An optically elongated and not very centrally concentrated quasar. The optical and radio emissions may have similar shapes (de Vries et al. 1997).

*3C343.1* ( $z = 0.75$ ): No radio core has been detected (Ludke et al. 1998).

*3C345* ( $z = 0.595$ ): A superluminal optically violently variable quasar (Penston & Cannon 1970, Katajainen et al. 2000). The spectrum is flat for wavelengths  $> 3\text{mm}$  and steepens for  $\lambda \leq 3\text{mm}$  (Rantakyroo et al. 1998). As NED coordinates are uncertain by  $3''$  we use for astrometry the VLA map by Leahy & Perley (1991).

*3C346* ( $z = 0.162$ ): Narrow-line radio galaxy showing both extended and compact X-ray emission (Hardcastle & Worrall 1999). In the optical there is a jet and a bright core (de Koff et al. 1996). We ignore deviant fluxes by Morabito et al. (1982).

*3C349* ( $z = 0.205$ ): There are two companions, a faint filament suggests an interaction within the triple (Roche & Eales 2000).

*3C351* ( $z = 0.372$ ): Radio-loud QSO of moderate X-ray luminosity. The spectrum from  $0.3\text{--}10.1\mu\text{m}$  can be fitted with a broken power law (Neugebauer et al. 1987).

*3C356* ( $z = 1.079$ ): In the optical, there are two nuclei  $5''$  apart (McCarthy et al. 1995, 1997) and both are detected in the radio (Eales & Rawlings 1990, Fernini et al. 1993). We identify the one which is brighter in the K band with the nucleus of the radio source. 3C356 is detected at X-rays with ROSAT (Hardcastle & Worrall 1999, Crawford & Fabian 1996).

*3C368* ( $z = 1.131$ ): The spectrum from radio to optical wavelengths can be fit by a power-law with a break in the infrared. There are two knots emitting synchrotron emission in the optical (O'Dea et al. 1999). Near infrared spectroscopy by Jackson & Rawlings (1997) shows that the nucleus is contaminated by a galactic M star.

*3C371* ( $z = 0.051$ ): BL Lac object with an unresolved HST point source (Martel et al. 1999).

*3C379.1* ( $z = 0.256$ ): Shows extended OIII emission over a scale of  $9''$  (McCarthy et al. 1995).

*3C380* ( $z = 0.692$ ): There are two optical hot spots coinciding with radio peaks (Ludke et al. 1998). Therefore, the optical hot spots probably originate from synchrotron radiation (de Vries et al. 1997).

*3C381* ( $z = 0.161$ ): Shows extended OIII emission on a scale of  $\sim 20''$  (McCarthy et al. 1995). There is a low surface brightness companion  $5.5''$  away (Roche & Eales 2000).

*3C382* ( $z = 0.058$ ): A classic broad-lined radio galaxy whose optical luminosity is dominated by an extremely blue AGN (Roche & Eales 2000).

*3C386* ( $z = 0.017$ ): An elliptical with a compact optical nucleus. There are two point sources of similar magnitude  $\sim 3''$  away from the nucleus. They might be faint foreground stars or small companion galaxies (Martel et al. 1999).

*3C388* ( $z = 0.091$ ): This radio galaxy has an unresolved optical nucleus (Martel et al. 1999) and two companions with a nuclear separation of  $7''$  (Roche & Eales 2000). The X-ray images show significant diffuse emission (Hardcastle & Worrall 1999).

*3C390.3* ( $z = 0.056$ ): A double-lobed, broad line blazar (Fomalont et al. 2000) detected also at X-rays (Hardcastle & Worrall 1999). The optical band is dominated by a nuclear point source (Martel et al. 1999).

*3C401* ( $z = 0.201$ ): A radio galaxy with a double nucleus (separation  $3.6''$ ) and several neighbours (Roche & Eales 2000).

*3C402* ( $z = 0.025$ ): An elliptical galaxy with an FR I morphology and a double radio nucleus. There is a massive nuclear disk of gas and dust (De Juan et al. 1996).

*3C410* ( $z = 0.249$ ): An elliptical with an optical jet candidate (de Koff et al. 1996).

*3C418* ( $z = 1.69$ ): Has several nearby but faint companions (Lehnert et al. 1999).

*3C430* ( $z = 0.056$ ): An elliptical with a narrow, arc-shaped dust lane that slices the core (Martel et al. 1999).

*3C433* ( $z = 0.101$ ): For the near infrared we use the data of 2MASX J2123445+250427. The absorption map by de Koff et al. (2000) shows patchy dust features.

*3C442* ( $z = 0.026$ ): A galaxy pair interacting with NGC7237 (De Vaucouleurs et al. 1976).

*3C445* ( $z = 0.056$ ): A broad emission line object (Eracleous & Halpern 1994) with an unresolved nucleus (Martel et al. 1999).

*3C449* ( $z = 0.017$ ): A low-power radio galaxy with multiple X-ray components and a nearby companion (Worrall & Birkinshaw 2000). Leon et al. (2001) derived from CO a molecular gas mass of  $M(\text{H}_2) \sim 2.3 \times 10^8 M_{\odot}$ . The HST images reveals a  $5''$  inner disk-like feature (Zirbel & Baum 1998).

*3C452* ( $z = 0.081$ ): de Koff et al. (2000) find indication of a faint dust lane near the nucleus. The radio source has a bright core and two lobes.

*3C454.1* ( $z = 1.841$ ): This source appears in the radio as a double with no core (Ludke et al. 1998). In the optical continuum one sees two nuclear condensations separated by  $2''$  (Djorgovski et al. 1988).

*3C456* ( $z = 0.233$ ): The radio core of this FR II galaxy lies within  $1''$  of the optical core position (Harvanek & Hardcastle 1998). The near IR shows extended emission (de Vries et al. 1997).

*3C459* ( $z = 0.02$ ): This steep spectrum ULIRG (IRAS 23140+0348) shows optical absorption features suggestive of young stellar populations (Miller 1981) and broad wings on both  $H\alpha$  and  $H\beta$  (Yee & Oke 1978). In the optical there are two polarisation components (Draper et al. 1993) none of which coincide with the radio axis. The radio emission (Condon et al. 1998) is extended to only  $\sim 10''$  (48kpc).

*3C465* (NGC7720,  $z = 0.030$ ): HST reveals a dusty kpc-size disk (Martel et al. 1999) which is roughly perpendicular to the radio jets (de Koff et al. 2000).

*3C469.1* ( $z = 1.336$ ): There is a double nucleus in the optical not aligned with the radio axis (McCarthy et al. 1997).

*4C+72.26* ( $z = 3.536$ ): The galaxy with the greatest red shift in our sample.

*NGC5532NED02* ( $z \sim 0.0237$ ): As no redshift is found in NED we use the value for NGC5532 (3C296).

*NGC7236* ( $z = 0.026$ ): A peculiar radio galaxy merging with NGC7237. It is also detected at X-ray (Hardcastle & Worrall 1999).

*PMN J0214-1158* ( $z = 2.34$ ): A large high redshift radio source with a steep radio spectrum; simple double morphology and jet signatures (Roettgering et al. 1994).

*IRAS F 17130+5021* ( $z = 0.05$ ): A galaxy pair  $15''$  away associated with 2MASX J 1714167+501816.

## Appendix B: Notes on individual fits

*3C006.1*: Evidence for dust comes from ISOCAM  $12\mu\text{m}$  (this work) and weak millimeter detection by Haas et al. (2001). Evidence for hot dust comes from ISOCAM only.

*3C013 and 3C017*: Fitting the visible and ISOCAM data points by a Planck function requires a rest frame temperature of 2600 K. If one allows for moderate reddening of  $A_V = 1$  mag the temperature would rise to 2900 K. Such a value is still lower than the expected mean stellar temperature in the galaxy and therefore the presence of hot dust is likely.

*3C018*:

*3C018*: IRAS fluxes suggests  $A_V$  larger than 30mag. Evidence for hot dust from ISOCAM only.

*3C020*: Evidence for hot dust by ISOCAM.

*3C022*: Fitting the visible and ISOCAM data points by a Planck function requires a rest frame temperature of 3000 K. If one allows for moderate reddening of  $A_V = 1$  mag in the galaxy the temperature would rise to 3600 K. Such a value is compatible to a normal stellar population. However, near IR imaging (Simpson et al. 1999) suggests a possible detection of dust.

*3C031*: ISOCAM emission comes from a compact region of about  $8''$  whereas the shown optical data are the magnitudes of the whole galaxy ( $180''$ ). The MIR emission of the stars are therefore only a small contribution to the ISOCAM fluxes. Evidence for hot dust by ISOCAM.

*3C033.1, 3C048 and 3C061.1*: Evidence for dust by ISOCAM and ISOPHOT.

*3C66B*: Evidence for hot dust comes from ISOCAM data.

*3C079*: Evidence for dust from ISOCAM and ISOPHOT.

*3C083.1*: Star superposed just  $3''$  southeast of the nucleus makes modelling of this galaxy impossible.

*3C098*: Evidence for hot dust from ISOCAM only.

*3C231*: M82 starburst model as described by Krügel & Siebenmorgen (1994).

*3C249.1*: Evidence for dust from ISOCAM and ISOPHOT.

*3C265*: Evidence for dust from ISOCAM only.

*3C270*: No evidence of dust from ISOCAM.

*3C272.1*: Evidence for dust from ISOPHOT only (Haas et al. 2001).

*3C273*: Possible hot dust detection by ISOCAM.

*3C274*: No evidence of dust from ISOCAM.

*3C277.3*: Evidence for dust from ISOCAM only.

*3C286*: Evidence for hot dust by ISOCAM only.

*3C288.1*: IRAS  $60\mu\text{m}$  maybe due to confusion. Likely detection of hot dust by ISOCAM.

*3C293*: Evidence for hot dust from ISOCAM only.

*3C295*: Evidence for dust from ISOCAM and ISOPHOT.

*3C296*: IRAS  $100\mu\text{m}$  maybe due to confusion. Likely detection of hot dust by ISOCAM.

*3C303.1*: Fitting the visible and ISOCAM data points by a Planck function requires a rest frame temperature of 2600 K. If one allows for moderate reddening of  $A_V = 1$  mag the temperature would rise to 2900 K. Such a value is still lower than the expected mean stellar temperature in the galaxy. Evidence for dust from ISOCAM and ISOPHOT.

*3C305*: Evidence for dust by ISOCAM and ISOPHOT.

*3C309.1*: Evidence for dust by ISOCAM and ISOPHOT.

*3C319*: Likely detection of hot dust by ISOCAM.

*3C321*: Evidence for dust from ISOCAM and ISOPHOT.

*3C324*: Evidence of hot dust from ISOCAM only.

*3C330*: Evidence for dust from ISOCAM only.

*3C332*: Evidence for hot dust from ISOCAM only.

*3C336*: Evidence for hot dust from ISOCAM only.

*3C338*: Evidence for dust from IRAS only.

*3C341*: Evidence for dust from ISOCAM only.

*3C343*: Possible detection of dust by ISOCAM only.

*3C345*: Evidence for hot dust from ISOCAM only.

*3C346*: Evidence for dust from ISOCAM only. Large deviation with ISOPHOT  $12\mu\text{m}$  fluxes given by Haas et al. (2001).

*3C349*: Evidence for dust from ISOCAM only.

*3C351*: Evidence for dust from ISOCAM and ISOPHOT.

*3C356*: Evidence for dust from ISOCAM and ISOPHOT.

*3C371*: No evidence for dust since the contribution of the synchrotron radiation to the ISOCAM data is unclear.

*3C379.1*: Evidence for dust by ISOCAM only.

*3C380*: The measured radio core flux is similar to the total radio emission, so that the synchrotron component, interpolated to the IR, is strong. Still the ISOCAM detection gives evidence of dust emission.

*3C381*: Evidence for dust from ISOCAM and ISOPHOT.

*3C386*: Evidence for dust from ISOCAM at  $14.3\mu\text{m}$  only.

*3C401*: In the infrared/submillimeter there are only upper limits which hints to model this galaxy.

*3C402*: ISOCAM emission comes from a compact region of about  $9''$  whereas the shown optical data are the magnitudes of the whole galaxy ( $55''$ ). The MIR emission of the stars is therefore only a small contribution to the ISOCAM fluxes. Evidence for dust from ISOPHOT (Haas et al. 2001) only.

*3C410*: Evidence for dust from ISOCAM only.

*3C442*: ISOCAM emission comes from a compact region ( $< 5''$ ) whereas the shown optical data are the magnitudes of the whole galaxy ( $130''$ ). The MIR emission of the stars is therefore only a small contribution to the ISOCAM fluxes. Weak  $12\mu\text{m}$  detection might be still photospheric. No evidence for dust.

*3C449*: ISOCAM emission comes from a compact region of about  $7''$  whereas the shown optical data are the magnitudes of the whole galaxy ( $90''$ ). The MIR emission of the stars is therefore only a small contribution to the ISOCAM fluxes. Evidence for dust comes from ISOCAM only.

*3C449*: Evidence for hot dust from ISOCAM only.

*3C452*: Evidence for dust comes from ISOCAM only.

*3C456*: Fitting the visible and ISOCAM data points by a Planck function requires a rest frame temperature of 2300 K. If one allows for moderate reddening of  $A_V = 1$  mag the temperature would rise to 2600 K. Such a value is still lower than the expected mean stellar temperature in the galaxy. Evidence for dust from ISOCAM only.

*3C459*: Evidence for dust from ISOCAM and ISOPHOT.

*3C465*: ISOCAM emission comes from a compact region of about  $10''$  whereas the shown optical data are the magnitudes of the whole galaxy ( $180''$ ). The MIR emission of the stars is therefore only a small contribution to the ISOCAM fluxes. Evidence for hot dust from ISOCAM only.

*3C469.1*: Evidence for dust from ISOCAM and ISOPHOT.

*4C+72.26*: Our highest redshift quasar ( $z=3.532$ ). The photospheric contribution is unknown, so that there is yet no evidence for dust. The model is not well constrained by the sparse infrared/submillimeter data.

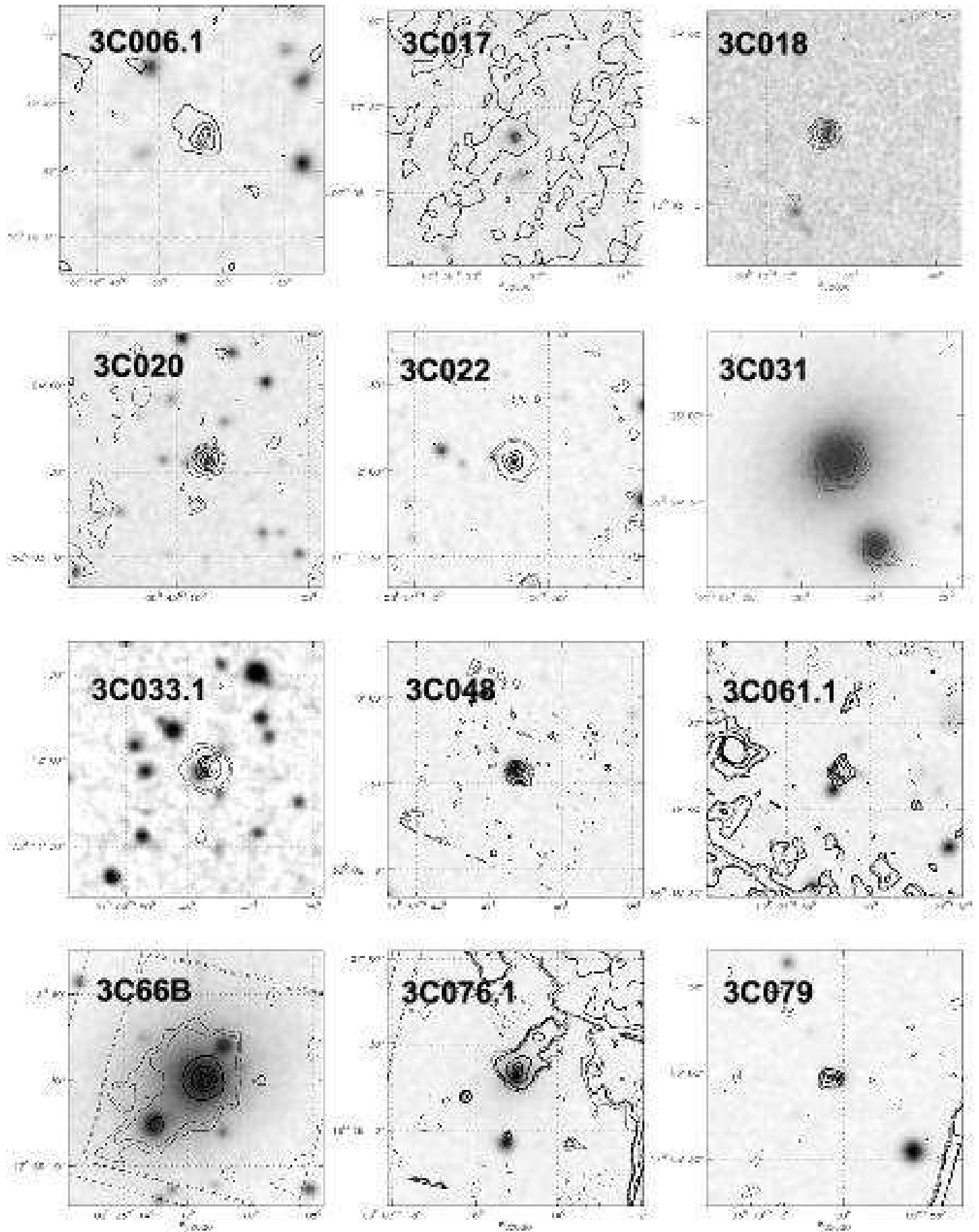


Fig. B.1. ISOCAM contours overlaid on DSS grey scale images centered on NED position of the object marked in

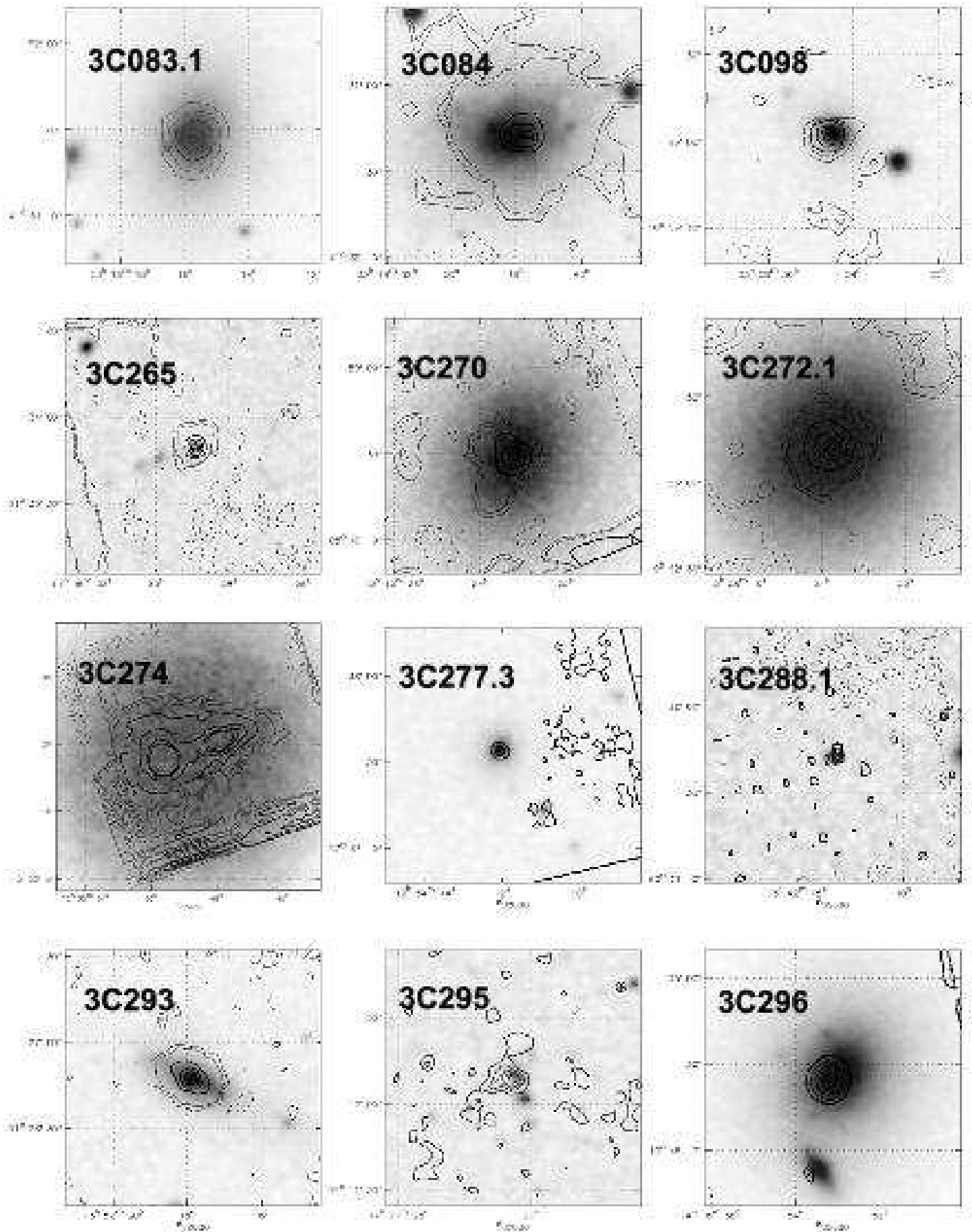


Fig. B.1. – continued –: **3C079** at  $12.0\mu\text{m}$  (LW10):  $\pm 89.6, \pm 106.7, 213.5, 320.2, 384.3$ . **3C083.1** at  $4.5\mu\text{m}$  (LW1):

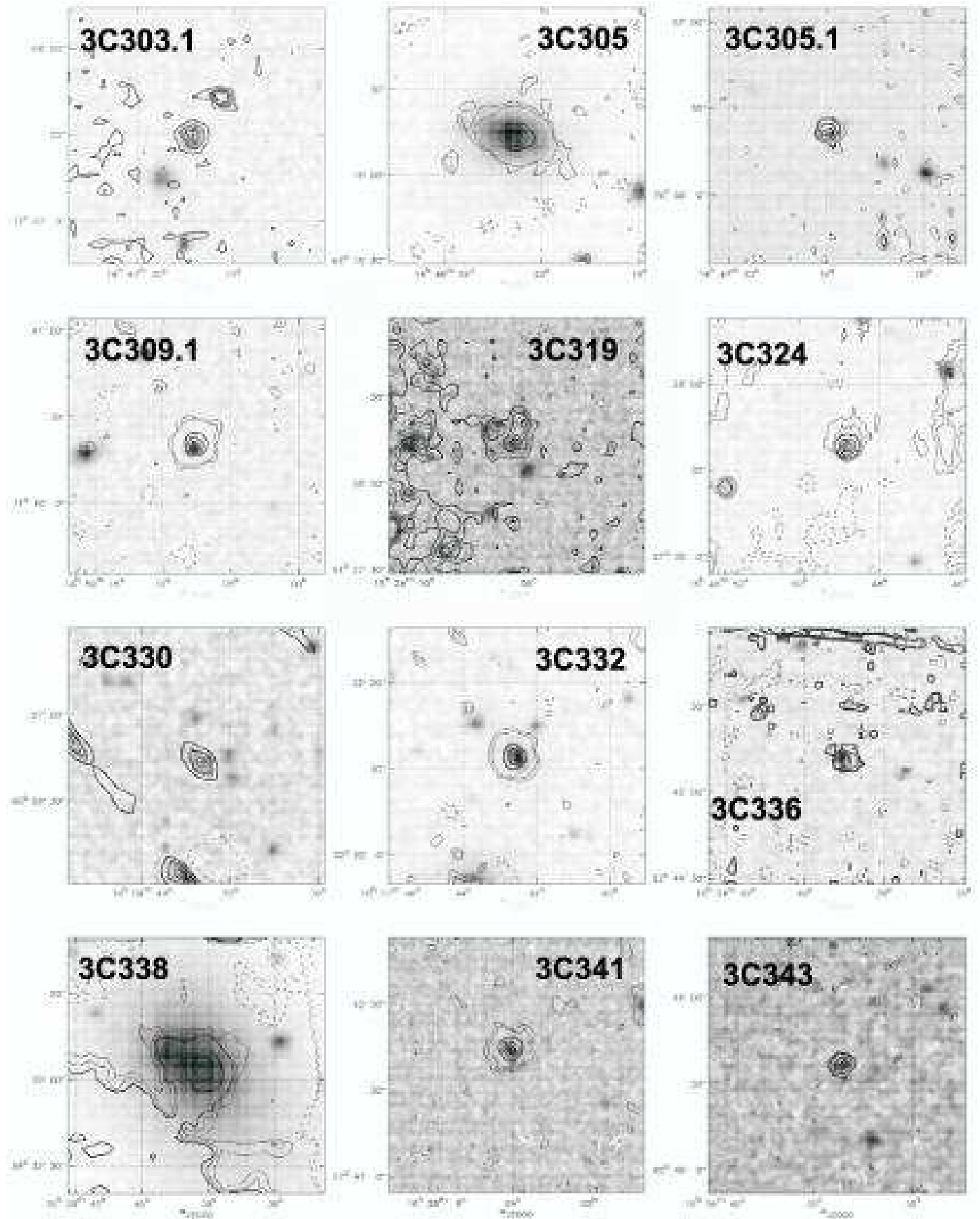


Fig. B.1. – continued –: 3C303.1 at  $12.0\mu\text{m}$  (LW10):  $\pm 5.0$ ,  $\pm 10.0$ , 17.9, 117.5, 176.3 3C305.0 at  $12.0\mu\text{m}$  (LW10):

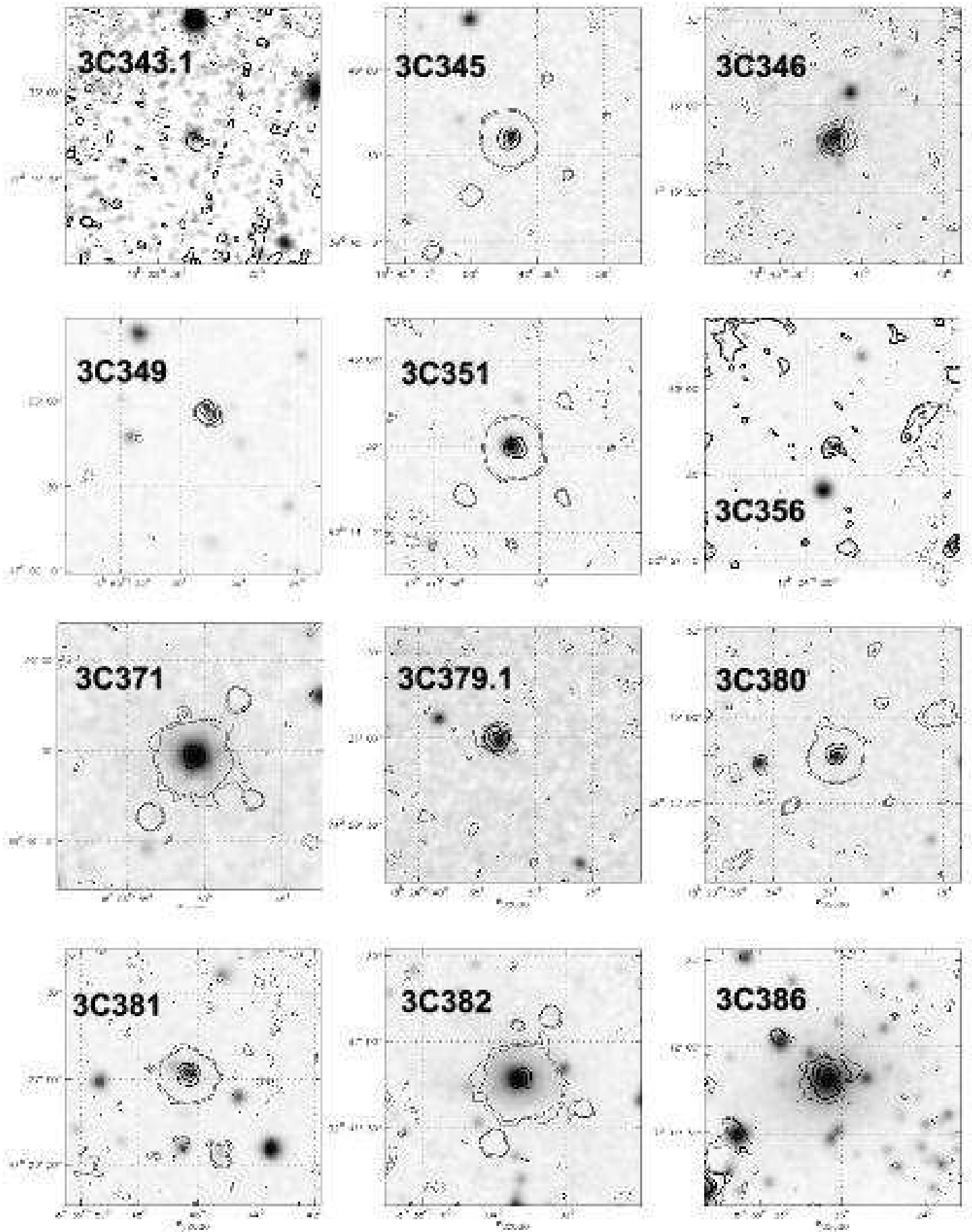


Fig. B.1. — (left) 3C343.1,  $z = 19.0$ ,  $(LW10) = 10.0$ ,  $15.7$ ,  $10.9$ ,  $50.0$ ,  $89.9$ ; (middle) 3C345,  $z = 19.0$ ,  $(LW10) = 110.1$

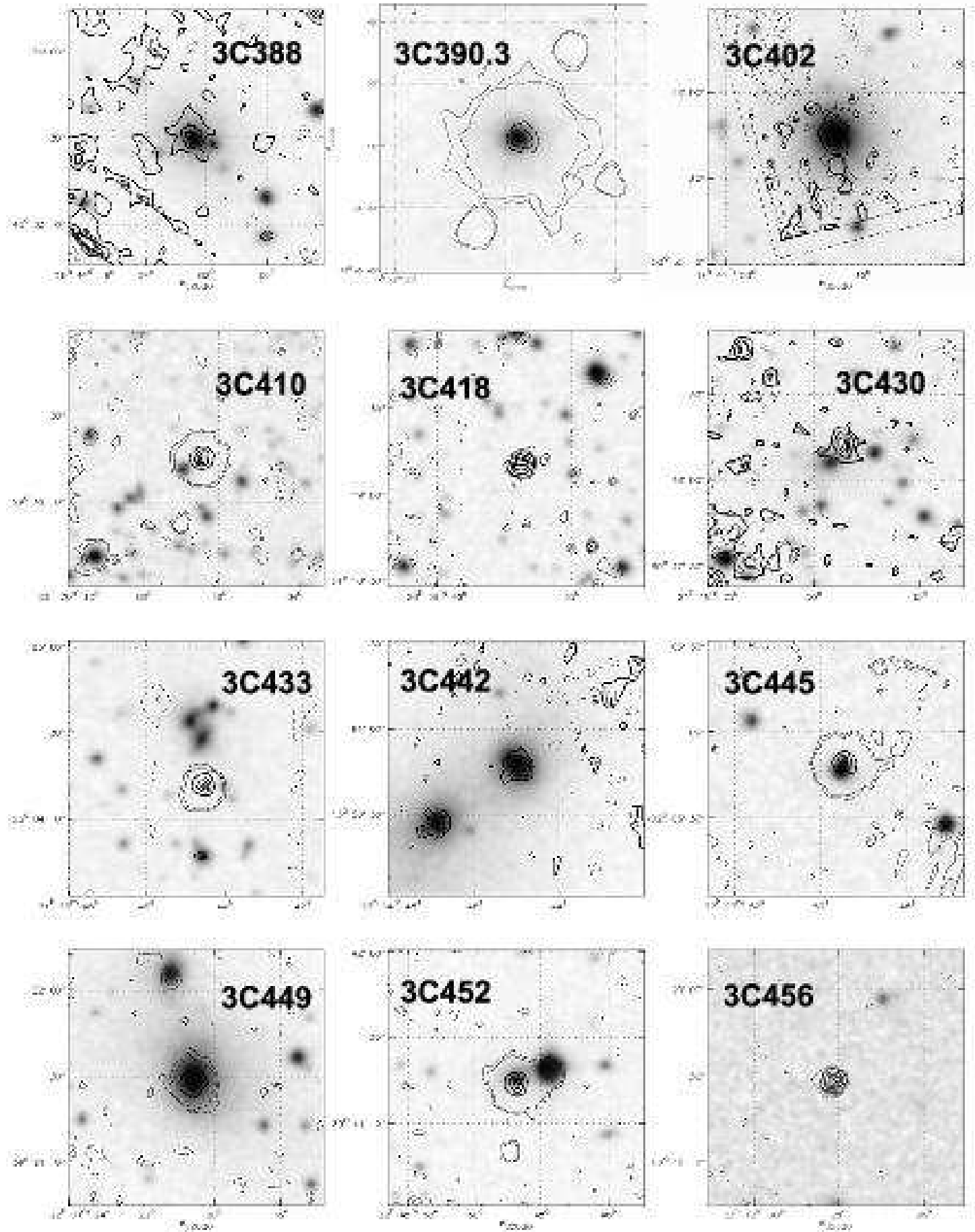
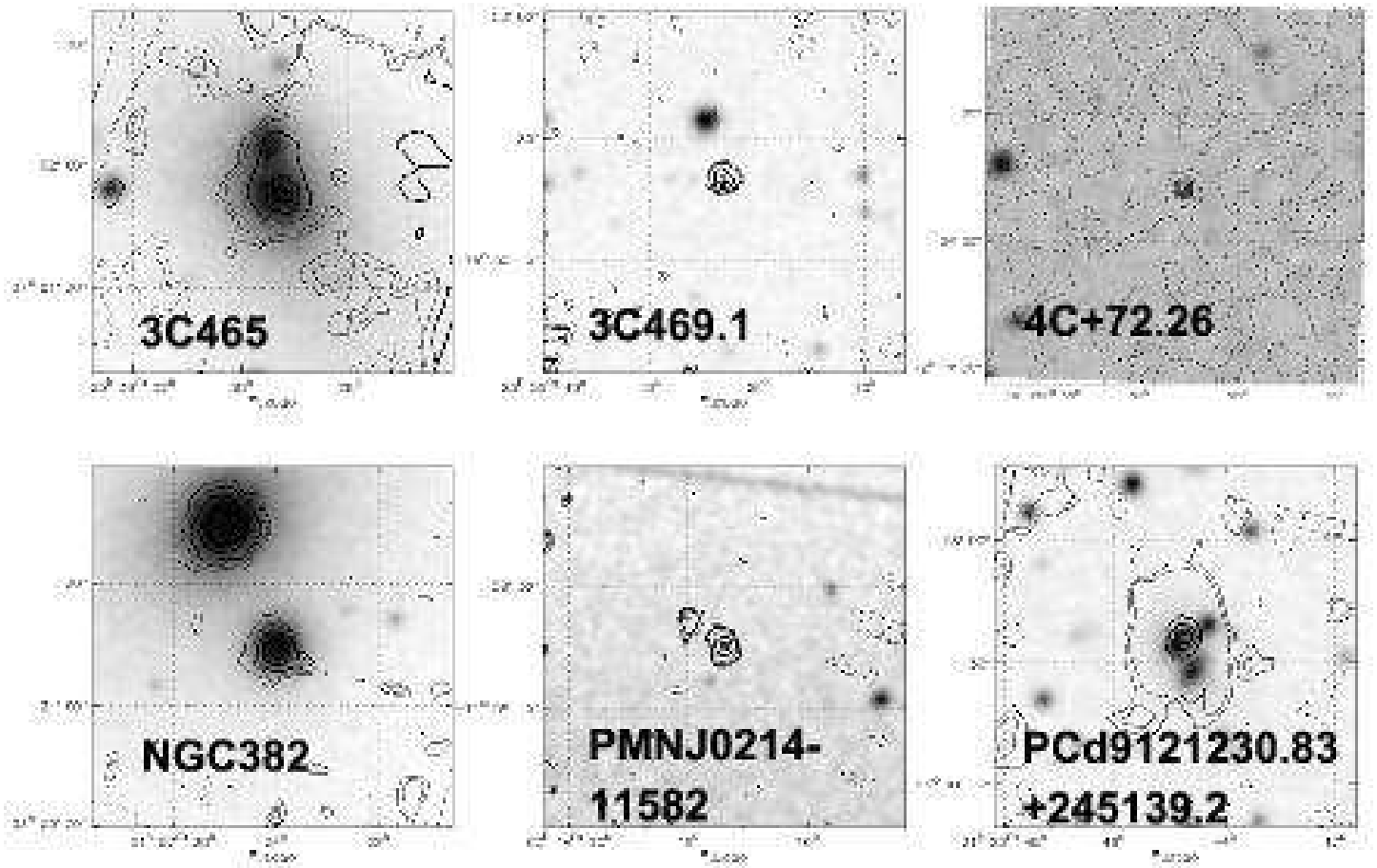


Fig. B.1. Continuum images of 3C388 + 19.0 (LW10), 3C390.3 + 19.0 (LW10), 3C402 + 19.0 (LW10), 3C410 + 19.0 (LW10), 3C418 + 19.0 (LW10), 3C430 + 19.0 (LW10), 3C433 + 19.0 (LW10), 3C442 + 19.0 (LW10), 3C445 + 19.0 (LW10), 3C449 + 19.0 (LW10), 3C452 + 19.0 (LW10), 3C456 + 19.0 (LW10).



**Fig. B.1.** – continued –: **3C465** at  $6.7\mu\text{m}$  (LW2):  $\pm 9.2, \pm 9.9, 19.7, 29.6, 35.5$ . **3C469.1** at  $12.0\mu\text{m}$  (LW10):  $\pm 10.3, \pm 20.7, 37.2, 181.7, 272.5$ . **4C+72.26** at  $12.0\mu\text{m}$  (LW10):  $\pm 0.4, \pm 0.7, 1.3, 114.0, 171.1$ . **NGC382** at  $12.0\mu\text{m}$  (LW10):  $\pm 27.3, \pm 54.6, 98.3, 173.4, 260.1$ . **PMNJ0214-11582** at  $12.0\mu\text{m}$  (LW10):  $\pm 4.6, \pm 9.1, 16.4, 250.0, 375.0$ . **PCd9121230.83+245139.2** at  $6.7\mu\text{m}$  (LW2):  $\pm 48.2, \pm 72.3, 235.9, 353.9, 424.6$ .

**Table B.1.** ISOCAM observations of 3CR sources ordered by TDT number.

1	2	3	4	5	6	7	8	9	10	11	12
TDT	RA J2000.0	Dec	Date UT	Filter	Lens "	$M$	$N$	$dM$ "	$dN$ "	$N_{\text{exp}}$	$t_{\text{int}}$ s
08800387	15 11 03.6	+07 49 52.9	13.02.96	LW10	6	2	2	180	180	8	2
10200421	18 05 06.7	+11 01 31.2	27.02.96	LW3	1.5	2	2	13.5	13	51	2
				LW2	1.5	2	2	13.5	13	51	2
10601408	16 28 38.6	+39 33 07.0	02.03.96	LW3	3	3	3	9	9	16	2
				LW1	3	3	3	9	9	12	5
12300106	09 55 51.7	+69 40 45.9	19.03.96	CVF	3	1	1	0	0	25	2
12300205	14 49 21.5	+63 16 13.6	19.03.96	LW3	3	3	3	15	15	49	2
				LW2	1.5	3	3	7.5	7	18	2
14301909	14 36 37.1	+63 19 13.8	08.04.96	LW10	3	5	5	144	144	44	5
14302010	14 36 37.1	+63 19 13.8	08.04.96	LW10	3	5	5	144	144	44	5
18001405	14 11 20.6	+52 12 08.6	15.05.96	LW3	3	4	4	144	144	30	10
				LW2	3	4	4	144	144	30	10
21305001	11 04 13.8	+76 58 57.3	17.06.96	CVF	6	1	1	0	0	14	10
22201802	11 45 28.6	+31 33 49.1	26.06.96	LW2	3	5	5	9	9	13	10
22400303	11 45 28.6	+31 33 49.1	28.06.96	LW10	3	7	7	6	6	15	10
22400201	11 45 28.6	+31 33 49.1	27.06.96	LW1	3	5	5	9	9	19	10
22801205	12 19 23.2	+05 49 29.4	02.07.96	LW3	3	3	3	9	9	12	2
				LW2	3	3	3	9	9	12	2
23100414	12 25 03.7	+12 53 14.0	05.07.96	LW7	3	5	5	9	9	4	5
				LW3	3	5	5	9	9	4	5
				LW2	3	5	5	9	9	3	20
23502406	12 25 03.6	+12 53 14.1	09.07.96	LW1	6	2	2	108	108	25	5
23800308	12 30 49.4	+12 23 28.1	12.07.96	LW1	6	2	2	108	108	25	5
				LW2	3	2	2	54	54	18	5
				LW3	6	2	2	108	108	23	2
23901834	12 30 48.6	+12 23 33.0	13.07.96	LW10	1.5	3	3	4.5	4	10	5
24100504	12 28 46.8	+02 08 07.9	14.07.96	LW3	1.5	1	1	0	0	508	5
				LW2	1.5	1	1	0	0	629	5
24201104	12 45 38.4	+03 23 20.3	16.07.96	LW10	3	5	5	144	144	27	5
24407233	13 42 13.2	+60 21 42.0	18.07.96	LW10	3	2	2	60	60	5	10
24500106	12 54 12.0	+27 37 33.5	18.07.96	LW3	3	3	3	15	15	45	5
				LW2	1.5	3	3	7.5	7	22	5
27000606	14 16 52.8	+10 48 23.0	13.08.96	LW2	3	3	3	9	9	12	2
				LW3	3	3	3	9	9	12	2
27503920	14 36 43.1	+15 44 13.0	17.08.96	LW10	3	5	5	144	144	32	5
30300511	15 49 48.9	+21 25 38.8	14.09.96	LW1	3	5	5	9	9	36	10
30300612	15 49 48.9	+21 25 38.8	14.09.96	LW2	3	5	5	9	9	22	10
30400442	16 24 39.0	+23 45 13.0	15.09.96	LW10	3	2	2	60	60	5	10
30492200	16 24 39.5	+23 45 00.6	16.09.96	LW2	6	1	1	0	0	6	25.2
33600323	16 09 36.5	+65 56 49.0	17.10.96	LW3	6	4	4	504	504	24	10
				LW2	6	4	4	504	504	24	10
35200533	19 59 25.8	+40 44 11.0	02.11.96	LW2	1.5	3	3	4.5	4	9	10
35701635	21 23 44.5	+25 04 10.0	08.11.96	LW2	3	4	4	9	9	8	10
36701710	22 31 20.5	+39 21 30.0	18.11.96	LW3	3	3	3	9	9	13	2
				LW2	3	3	3	9	9	13	2
37403041	22 31 20.5	+39 21 30.0	25.11.96	LW10	6	4	4	36	36	9	10
37500303	23 16 34.5	+04 05 17.4	25.11.96	LW1	6	1	1	0	0	12	5
				LW4	6	1	1	0	0	12	5
				LW6	6	1	1	0	0	12	5
				LW3	6	1	1	0	0	12	5
38600922	16 24 39.5	+23 45 00.6	10.07.97	LW2	6	1	1	0	0	7	25.2
38800808	13 31 08.2	+30 30 33.0	08.12.96	LW10	3	1	1	0	0	206	2
39501112	23 38 29.4	+27 01 54.0	15.12.96	LW3	3	3	3	9	9	16	2
				LW2	3	3	3	9	9	16	2

Table B.1. continued

1	2	3	4	5	6	7	8	9	10	11	12
TDT	RA J2000.0	Dec	Date UT	Filter	Lens "	$M$	$N$	$dM$ "	$dN$ "	$N_{\text{exp}}$	$t_{\text{int}}$ s
39901248	16 38 28.1	+62 34 44.0	19.12.96	LW10	3	2	2	60	60	5	10
40100319	14 36 43.1	+15 44 13.0	21.12.96	LW10	3	5	5	144	144	32	5
40201422	01 07 27.4	+32 24 08.0	22.12.96	LW2	6	3	3	36	36	9	10
41907203	00 06 22.6	-00 04 25.0	08.01.97	LW10	3	2	2	60	60	5	10
43502724	02 23 11.5	+42 59 30.0	24.01.97	LW2	3	2	3	9	9	8	10
43901804	01 37 41.2	+33 09 35.3	29.01.97	LW3	1.5	2	2	22.5	22	20	5
45304902	02 23 11.5	+42 59 30.0	11.02.97	LW3	3	3	3	9	9	10	2
				LW1	3	3	3	9	9	8	5
46300408	14 49 21.5	+63 16 14.0	21.02.97	LW1	3	3	3	9	9	8	5
46601603	03 03 15.0	+16 26 16.0	24.02.97	LW2	3	3	3	9	9	8	2
				LW3	3	3	3	9	9	9	2
				LW1	3	3	3	9	9	7	5
47100710	18 38 25.4	+17 11 52.0	01.03.97	LW2	3	3	3	9	9	15	2
				LW3	3	3	3	9	9	15	2
49604639	19 41 42.8	+50 36 36.7	26.03.97	LW10	3	3	3	72	72	15	5
50304334	18 33 45.9	+47 27 01.2	02.04.97	LW10	3	3	3	72	72	15	5
51100561	16 28 38.3	+39 33 04.5	10.04.97	LW10	3	3	3	72	72	15	5
51100679	16 42 58.7	+39 48 36.7	10.04.97	LW10	3	3	3	72	72	15	5
51301035	18 38 26.3	+17 11 49.5	12.04.97	LW10	3	3	3	72	72	15	5
51400760	14 49 21.8	+63 16 14.0	13.04.97	LW10	3	3	3	72	72	15	5
51800103	17 14 11.9	+50 16 60.0	17.04.97	LW10	6	11	11	198	198	12	5
51800667	17 10 44.0	+46 01 29.1	17.04.97	LW10	3	3	3	72	72	15	5
51800831	17 28 20.1	+31 46 01.9	17.04.97	LW10	3	3	3	72	72	15	5
52100668	17 24 19.3	+50 57 36.1	20.04.97	LW10	3	3	3	72	72	15	5
52100804	17 14 11.9	+50 16 60.0	20.04.97	LW10	6	11	11	198	198	12	5
52201845	21 23 44.0	+25 04 31.1	21.04.97	LW10	3	3	3	72	72	15	5
52201948	21 44 11.6	+28 10 18.7	21.04.97	LW10	3	3	3	72	72	15	5
52500130	17 04 41.3	+60 44 30.1	24.04.97	LW10	3	3	3	72	72	15	5
52500429	16 59 28.8	+47 02 55.4	24.04.97	LW10	3	3	3	72	72	15	5
52500562	18 35 03.3	+32 41 46.9	24.04.97	LW10	3	3	3	72	72	15	5
52900115	14 43 14.6	+77 07 27.6	28.04.97	LW10	3	3	3	72	72	15	5
52900417	15 10 23.0	+70 45 52.8	28.04.97	LW10	3	3	3	72	72	15	5
52901232	18 06 50.5	+69 49 29.9	28.04.97	LW10	3	3	3	72	72	15	5
52901433	18 24 32.8	+74 20 57.2	28.04.97	LW10	3	3	3	72	72	15	5
52901537	18 42 08.7	+79 46 17.8	28.04.97	LW10	3	3	3	72	72	15	5
52902663	21 04 06.3	+76 33 11.8	28.04.97	LW10	3	3	3	72	72	15	5
53200838	19 40 24.9	+60 41 36.7	01.05.97	LW10	3	3	3	72	72	15	5
53503041	20 20 06.5	+29 42 13.6	04.05.97	LW10	3	3	3	72	72	15	5
53503146	21 23 16.2	+15 48 05.6	04.05.97	LW10	3	3	3	72	72	15	5
53503288	21 47 25.1	+15 20 33.8	04.05.97	LW10	3	3	3	72	72	15	5
53702750	22 14 46.8	+13 50 27.1	06.05.97	LW10	3	3	3	72	72	15	5
53702911	22 14 46.9	+13 50 27.0	06.05.97	LW3	3	3	3	9	9	15	2
53702911	22 14 46.9	+13 50 27.0	06.05.97	LW2	3	3	3	9	9	15	2
54000949	21 55 52.1	+38 00 29.4	09.05.97	LW10	3	3	3	72	72	15	5
54100619	15 24 04.8	+54 28 05.2	10.05.97	LW10	3	3	3	72	72	15	5
54100836	18 44 02.3	+45 33 30.3	10.05.97	LW10	3	3	3	72	72	15	5
54100969	18 29 31.7	+48 44 46.3	10.05.97	LW10	3	3	3	72	72	15	5
54101870	20 38 36.8	+51 19 12.1	10.05.97	LW10	3	3	3	72	72	15	5
54301344	21 18 19.0	+60 48 08.2	12.05.97	LW10	3	3	3	72	72	15	5
54500518	22 23 49.5	-02 06 12.3	14.05.97	LW2	3	1	1	0	0	43	2
				LW3	3	1	1	0	0	49	2
54700854	23 12 28.1	+09 19 27.6	16.05.97	LW10	3	3	3	72	72	15	5
54801053	22 45 48.7	+39 41 16.6	17.05.97	LW10	3	3	3	72	72	15	5
54801112	22 31 20.5	+39 21 30.0	17.05.97	LW1	3	3	3	9	9	8	5

Table B.1. continued

1	2	3	4	5	6	7	8	9	10	11	12
TDT	RA J2000.0	Dec	Date UT	Filter	Lens "	$M$	$N$	$dM$ "	$dN$ "	$N_{\text{exp}}$	$t_{\text{int}}$ s
54801252	22 31 20.5	+39 21 29.4	17.05.97	LW10	3	3	3	72	72	15	5
55500476	18 06 50.8	+69 49 30.0	24.05.97	LW3	3	1	1	0	0	109	2
56001074	22 50 32.9	+71 29 19.0	29.05.97	LW10	3	3	3	72	72	15	5
56201064	23 55 23.0	+79 55 18.7	31.05.97	LW10	3	3	3	72	72	15	5
56201411	02 22 36.2	+86 19 07.6	31.05.97	LW10	3	3	3	72	72	15	5
56500458	23 38 29.4	+27 01 53.3	03.06.97	LW10	3	3	3	72	72	15	5
56501357	23 21 28.5	+23 46 47.2	03.06.97	LW10	3	3	3	72	72	15	5
57502102	00 38 20.5	-02 07 40.8	13.06.97	LW10	3	3	3	72	72	15	5
58703793	01 07 24.9	+32 24 44.9	25.06.97	LW10	3	3	3	72	72	15	5
58703801	01 07 25.0	+32 24 45.2	25.06.97	LW3	3	3	3	9	9	9	2
59501620	15 31 25.4	+35 33 40.5	03.07.97	LW10	3	3	3	72	72	15	5
59601514	02 14 17.4	-11 58 46.2	04.07.97	LW10	3	8	8	36	36	13	5
59601615	02 14 17.4	-11 58 46.2	04.07.97	LW10	3	8	8	36	36	12	5
59702305	00 43 09.2	+52 03 33.7	05.07.97	LW10	3	3	3	72	72	15	5
59702607	01 09 44.3	+73 11 57.6	05.07.97	LW10	3	3	3	72	72	15	5
60001373	16 09 34.6	+65 56 37.7	08.07.97	LW10	3	3	3	72	72	15	5
60001472	14 59 07.5	+71 40 19.5	08.07.97	LW10	3	3	3	72	72	15	5
60009220	14 59 13.5	+71 40 26.9	08.07.97	LW2	6	1	1	0	0	7	25.2
60201626	16 28 03.8	+27 41 38.6	10.07.97	LW10	3	3	3	72	72	15	5
60201725	16 17 42.8	+32 22 28.6	10.07.97	LW10	3	3	3	72	72	15	5
61503617	03 19 48.2	+41 30 42.4	23.07.97	LW2	6	2	2	108	108	25	5
61503807	03 10 00.3	+17 05 54.0	23.07.97	LW10	3	1	1	0	0	61	2
61701307	13 52 17.8	+31 26 47.0	25.07.97	LW2	3	3	3	9	9	8	2
				LW3	3	3	3	9	9	9	2
61701413	13 52 17.8	+31 26 46.4	25.07.97	LW10	3	3	3	72	72	15	5
61900565	16 34 33.7	+62 45 36.2	27.07.97	LW10	3	3	3	72	72	15	5
61901003	00 40 50.3	+10 03 23.4	27.07.97	LW10	3	3	3	72	72	15	5
63301602	02 42 40.7	-00 00 47.3	10.08.97	LW1	3	2	2	36	36	247	2
63301902	02 42 40.7	-00 00 47.3	10.08.97	LW5	3	2	2	36	36	247	2
63302202	02 42 40.7	-00 00 47.3	10.08.97	LW9	3	2	2	36	36	266	2
63302405	03 58 54.7	+10 25 47.0	10.08.97	LW2	3	3	3	9	9	9	2
				LW3	3	3	3	9	9	8	2
64001327	16 43 48.7	+17 15 49.3	17.08.97	LW10	3	3	3	72	72	15	5
65800208	15 31 42.7	+24 04 24.7	03.09.97	CVF	3	1	1	0	0	33	2
65901032	03 18 15.7	+41 51 27.0	05.09.97	LW2	3	4	4	9	9	9	10
65901304	03 18 15.7	+41 51 27.0	05.09.97	LW3	3	3	3	9	9	9	2
70101081	00 16 31.1	+79 16 41.5	16.10.97	LW10	3	3	3	72	72	15	5
71200283	18 05 06.3	+11 01 31.2	27.10.97	LW2	1.5	1	1	0	0	83	5
				LW3	1.5	1	1	0	0	80	5
71702771	14 47 08.9	+76 56 19.6	01.11.97	LW10	3	3	3	72	72	15	5
74101506	19 08 23.7	+72 20 11.8	25.11.97	LW10	3	8	8	36	36	18	5
75300580	16 09 36.5	+65 56 42.7	07.12.97	LW3	6	20	3	228	18	15	5
75300681	16 09 36.5	+65 56 42.7	07.12.97	LW3	6	20	3	228	18	15	5
75300779	16 09 36.5	+65 56 42.7	07.12.97	LW3	6	20	3	228	18	15	5
75400182	16 09 36.5	+65 56 42.7	08.12.97	LW3	6	20	3	228	18	15	5
78500882	00 50 56.2	+51 12 03.8	08.01.98	LW10	3	3	3	72	72	15	5
80201405	03 18 12.1	-25 35 09.0	25.01.98	LW10	3	6	6	72	72	15	5
80201507	03 18 12.1	-25 35 09.0	25.01.98	LW10	3	6	6	72	72	14	5
80801283	00 34 14.7	+39 24 13.7	31.01.98	LW10	3	3	3	72	72	15	5